



3-Cm Fine Structure Masers: A Unique Signature of Supermassive Black Hole Formation via Direct Collapse in the Early Universe

Citation

Dijkstra, Mark, Shiv Sethi, and Abraham Loeb. 2016. "3-Cm Fine Structure Masers: A Unique Signature of Supermassive Black Hole Formation via Direct Collapse in the Early Universe." *The Astrophysical Journal* 820 (1) (March 10): 10. doi:10.3847/0004-637x/820/1/10.

Published Version

10.3847/0004-637x/820/1/10

Permanent link

<http://nrs.harvard.edu/urn-3:HUL.InstRepos:32072407>

Terms of Use

This article was downloaded from Harvard University's DASH repository, and is made available under the terms and conditions applicable to Open Access Policy Articles, as set forth at <http://nrs.harvard.edu/urn-3:HUL.InstRepos:dash.current.terms-of-use#OAP>

Share Your Story

The Harvard community has made this article openly available.
Please share how this access benefits you. [Submit a story](#).

[Accessibility](#)

3-CM FINE STRUCTURE MASERS: A UNIQUE SIGNATURE OF SUPERMASSIVE BLACK HOLE FORMATION VIA DIRECT COLLAPSE IN THE EARLY UNIVERSE

MARK DIJKSTRA¹, SHIV SETHI² & ABRAHAM LOEB³

¹Institute of Theoretical Astrophysics, University of Oslo, P.O. Box 1029 Blindern, N-0315 Oslo, Norway

²Raman Research Institute, C V Raman Avenue, Bangalore-560080, India and

³Harvard Smithsonian Center for Astrophysics, 60 Garden St, Cambridge, MA, 02138, USA

Draft version January 20, 2016

ABSTRACT

The direct collapse black hole (DCBH) scenario describes the isothermal collapse of a pristine gas cloud directly into a massive, $M_{\text{BH}} = 10^4\text{--}10^6 M_{\odot}$ black hole. In this paper we show that large HI column densities of primordial gas at $T \sim 10^4$ K with low molecular abundance—which represent key aspects of the DCBH scenario—provide optimal conditions for pumping of the $2p$ -level of atomic hydrogen by trapped Ly α photons. This Ly α pumping mechanism gives rise to inverted level population of the $2s_{1/2} - 2p_{3/2}$ transition, and therefore to stimulated fine structure emission at $\lambda = 3.04$ cm (rest-frame). We show that simplified models of the DCBH scenario amplify the CMB by up to a factor of $\sim 10^5$, above which the maser saturates. Hyperfine splitting of the 3-cm transition gives rise to a characteristic broad (FWHM \sim tens of MHz in the observers frame) asymmetric line profile. This signal subtends an angular scale of $\sim 1\text{--}10$ mas, which translates to a flux of $\sim 0.3\text{--}3 \mu\text{Jy}$, which is detectable with ultra-deep surveys being planned with SKA1-MID. While challenging, as the signal is visible for a fraction of the collapse time of the cloud, the matching required physical conditions imply that a detection of the redshifted 3-cm emission line would provide direct evidence for the DCBH scenario.

Subject headings: .cosmology–theory–quasars–high redshift

1. INTRODUCTION

The origin of supermassive black holes (SMBHs) in the Universe—especially those at $z \gtrsim 6$ (e.g. Fan et al. 2001; Willott et al. 2009; Mortlock et al. 2011; Venemans et al. 2013)—is still not understood (see e.g. Volonteri & Bellovary 2012; Haiman 2013). The ‘Direct Collapse Black Holes’ (DCBH) scenario provides an intriguing possibility in which primordial gas inside dark matter halos with $T_{\text{vir}} \geq 10^4$ K collapses *directly* into a $\sim 10^4\text{--}10^6 M_{\odot}$ black hole, without any intermediate star formation. DCBH formation requires primordial gas to collapse isothermally at $T \sim 10^4$ K (e.g. Bromm & Loeb 2003), which has been shown to prevent fragmentation (e.g. Li et al. 2003; Omukai et al. 2005).

Isothermal collapse at $T \sim 10^4$ K is possible if primordial gas is prevented from forming molecular hydrogen (H_2 , which acts as a gas coolant) during collapse. Formation of H_2 is prevented if the gas is bathed in a strong photo dissociating background (e.g. Bromm & Loeb 2003). Photodissociation occurs via (i) direct photodissociation by Lyman-Werner (LW) radiation ($E = 10.2\text{--}13.6$ eV), or (ii) indirect photodissociation through photo-detachment of H^- , which catalyses the formation of H_2 , by infrared (IR) radiation ($E > 0.76$ eV). DCBH formation therefore requires the collapse of

primordial gas inside atomically cooling halos, exposed to an intense Lyman-Werner and/or IR radiation fields. It is also possible to achieve near isothermal collapse with $T \sim 10^4$ K if the primordial haloes are threaded with (comoving) primordial magnetic fields of nano-Gauss strength (Sethi et al. 2010; Van Borm & Spaans 2013).

The DCBH formation process is a remarkably complex problem, which involves the hydrodynamics of gas collapsing from \sim a few kpc size down to event horizon of the black hole (see Bromm & Loeb 2003; Latif et al. 2013; Fernandez et al. 2014; Regan et al. 2014; Latif & Volonteri 2015, for hydrodynamical simulations of this process). In addition, the ‘critical’ intensity of radiation background, indicated with J_{crit} , that is needed to keep the gas free of H_2 depends on the precise spectral shape of the radiation background (including even the X-ray band, see e.g. Omukai et al. 2005; Shang et al. 2010; Wolcott-Green et al. 2011; Sugimura et al. 2014; Inayoshi & Tanaka 2015; Agarwal et al. 2015a). Because J_{crit} typically greatly exceeds that of the cosmic background, DCBH formation requires a nearby galaxy to boost the intensity of the local radiation field (Dijkstra et al. 2008b; Agarwal et al. 2012; Visbal et al. 2014a,b). This implies that the LW-radiation field is not isotropic, which also affects the value of J_{crit} (Regan et al. 2014). Furthermore, the spectral dependence of J_{crit} implies that J_{crit} depends on the stellar populations of the nearby galaxy (Agarwal et al. 2015a).

¹ mark.dijkstra@astro.uio.no

² sethi@rri.res.in

Finally, the close proximity to a star forming galaxies makes it more complicated to prevent enrichment of the gas by feedback-driven outflows originating from the nearby galaxy. It has been shown that small uncertainties in these processes can lead to orders of magnitude changes in the predicted number density of DCBHs (Dijkstra et al. 2008a, 2014).

Because of the large theoretical uncertainties associated with DCBH formation, it is extremely valuable to have observational signposts on this process. Agarwal et al. (2013) have presented predictions for the broad-band colours of DCBH host galaxies, under the assumption that the spectrum emitted by the accretion disk surrounding the DCBH is a multi-colored disk. Under this assumption, DCBH host galaxies are characterised by blue UV slopes ($\beta \sim -2.3$), which are similar to those predicted for metal poor, young stars. Inayoshi et al. (2015) more recently estimated the Ly α luminosity from the accretion flow onto the central black hole to be comparable to that of known Ly α emitting galaxies.

The goal of this paper is to focus on the two strongest *fine structure* lines of atomic hydrogen which include³: (i) the $2p_{1/2} \rightarrow 2s_{1/2}$ transition at $\lambda \approx 27$ cm ($\nu_{\text{ul}} = 1.1$ GHz), and (ii) the $2s_{1/2} \rightarrow 2p_{3/2}$ transition at $\lambda \approx 3.04$ cm ($\nu_{\text{ul}} = 9.9$ GHz) (see e.g. Wild 1952; Ershov 1987; Dennison et al. 2005; Sethi et al. 2007; Dijkstra et al. 2008b, for more details). It has long been realised that scattering of Ly α photons can “pump” the $2p$ -level, and give rise to stimulated 3-cm emission (e.g. Pottasch 1960; Field & Partridge 1961; Ershov 1987). These early studies focussed on pumping of the $2p$ -level in nearby HII regions, where Ly α scattering is limited by dust, and not nearly effective enough to give rise to stimulated 3-cm emission (Myers & Barrett 1972). However, the DCBH scenario is associated with primordial (i.e. dust-free) gas cloud with extremely large column densities of atomic hydrogen ($N_{\text{HI}} \gtrsim 10^{22} - 10^{24}$ cm⁻², also see Paccuci & Ferrara 2015) at $T \sim 10^4$ K. These conditions are ideal for Ly α photons to be both produced, and undergo a large number of scattering events, both of which are favourable for pumping the $2p$ -level of atomic hydrogen. Moreover, modelling of the relevant radiative processes is simplified in the absence of star formation & stellar feedback in the DCBH formation scenario. It is therefore highly timely to study the fine structure signatures of gas clouds directly collapsing into a black hole.

The 3-cm fine structure masers studied in this paper thus arise due to extremely efficient pumping by Ly α absorption of the excited upper level of the 3-cm transition. This pumping mechanism distinguishes the 3-cm maser from the more recently studied radio recombination line (RRL) masers (Strelitski et al. 1996; Spaans & Norman 1997). RRL masers can arise in the $n\alpha$ transitions (in which $\Delta n = 1$) for $n \gg 1$ due to collisional pumping: the efficiency with which electrons can excite these transitions increases as $\propto n^{4-5}$, while the spontaneous de-

cay rate between these transitions decreases as $n \propto n^{-5}$ (see Strelitski et al. 1996; Spaans & Norman 1997, for a more extended discussion).

The outline of this paper is as follows: § 2 describes our simplified model of the direct-collapse black hole scenario, the relevant processes that determine the $2s_{1/2}$ and $2p_{3/2}$ level populations and their fine-structure signatures. We present our main results in § 3. We discuss the detectability of stimulated fine structure emission in § 4. We discuss our model assumptions in § 5 before finally presenting our main conclusions in § 6. For completeness, in the concordance cosmology ($\Omega_{\text{m}} = 0.3, \Omega_{\Lambda} = 0.7, h = 0.7$) the mass of a dark matter halo with virial temperature of $T_{\text{vir}} = 10^4$ K is $M_{\text{tot}} = 10^8 (\mu/0.6)^{-3/2} ([1+z]/11)^{-3/2} M_{\odot}$, which has a virial radius of $r_{\text{vir}} = 1.8 ([1+z]/11)^{-1} (M_{\text{tot}}/10^8 M_{\odot})^{1/3}$ kpc (Barkana & Loeb 2001). The average number density of hydrogen atoms/nuclei at virialization is $\bar{n} = 0.048 ([1+z]/11)^3$ cm⁻³.

2. MODEL

2.1. Geometry

Our analysis is limited to spherically symmetric gas clouds with a uniform density. These simplifying assumptions offer us a clear view on the relevant radiative processes that determine whether the masing conditions exist. In particular, they allow us to treat the radiative transfer of Ly α photons analytically, which represents a major computational advantage. Under these assumptions the cloud is fully characterised by a single number density, n . For a given gas mass M_{gas} , this gives a cloud radius R . We discuss in § 5 how our main results are expected to be affected by these simplifying assumptions.

Hydrodynamical simulations indicate that that the gas density profile is closer to isothermal (i.e. $\rho(r) \propto r^{-2}$, e.g. Shang et al. 2010, Pacucci & Ferrara 2014). The gas density increases towards the centre of the collapsing gas cloud, which may lead to the formation of a quasi-star, a supermassive star, or a direct-collapse black hole in the centre of the cloud. We therefore also consider models in which the gas cloud contains a central source of ionising radiation, which represents a scenario in which a central black hole has already formed. Accretion rates onto the central black hole can be up to $\sim 0.1 M_{\odot} \text{ yr}^{-1}$ (e.g. Latif & Volonteri 2015), which can power a central source with a luminosity exceeding 10^{44} erg s⁻¹. We do not consider the hydrodynamic impact of the central source on the gas. Instead, we focus on the emission properties of gas with properties that were favourable for the DCBH scenario, i.e. the gas is pristine, no fragmentation occurred, and no stars have formed.

2.2. The Fine Structure Signal

We study the impact of the collapsing halo on CMB photons passing through them (see Fig 1). In general, a gas cloud with uniform density changes the CMB inten-

³ We adopted the notation nL_J , where n is the principle quantum number, L denotes the electron’s *orbital* angular momentum, and J denotes the *total* (orbital + spin) quantum number.

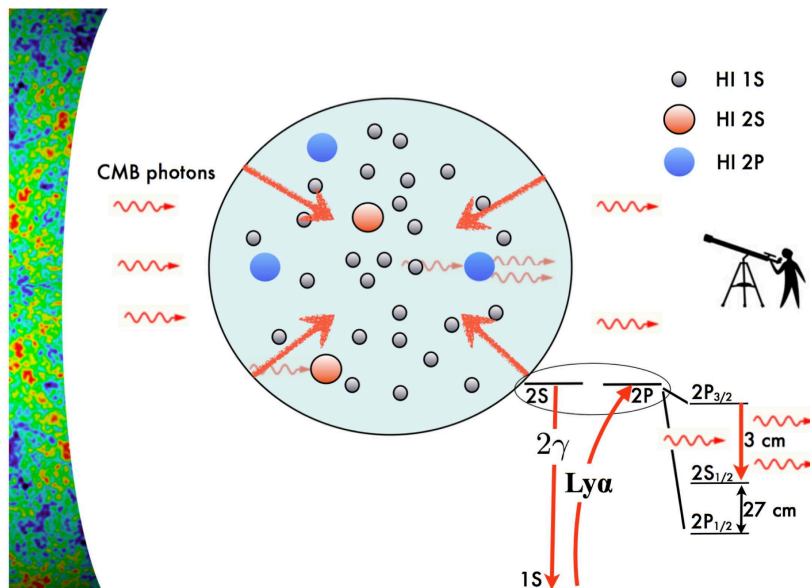


FIG. 1.— Schematic representation of the calculations in this paper. A gas cloud collapses directly into a ‘direct collapse black hole (DCBH). In the DCBH scenario, the gas cloud consists solely of atomic hydrogen gas (indicated by *circles*). The column density of atomic hydrogen, N_{HI} , is typically huge and can exceed $N_{\text{HI}} = 10^{24} \text{ cm}^{-2}$. Depending on the temperature of the cloud, a small fraction of atomic hydrogen is in the first excited state ($n = 2$, indicated by the *larger, colored circles*), which has two fine structure transitions at 1.1 GHz ($\lambda = 27 \text{ cm}$, $2p_{1/2} \rightarrow 2s_{1/2}$) and 9.9 GHz ($\lambda = 3 \text{ cm}$, $2s_{1/2} \rightarrow 2p_{3/2}$). These transitions are indicated in the lower right corner of the figure. In the case where the $2p_{3/2}$ is overpopulated with respect to $2s_{1/2}$, CMB radiation passing through the cloud induces stimulated emission in this transition. The *thick red arrows* indicate the maser cycle: Ly α pumps the $2p_{3/2}$ level. The CMB induces stimulated emission $2p_{3/2} \rightarrow 2s_{1/2}$, which is followed by decay to the ground state via two-photon emission.

sity, I_ν , by an amount

$$I_\nu(s) = I_{\nu,0} e^{-\kappa_\nu s} + \frac{j_\nu}{\kappa_\nu} (1 - e^{-\kappa_\nu s}), \quad (1)$$

at a distance s into the cloud. Here, $I_{\nu,0}$ denotes the intensity before entering the cloud, κ_ν denotes the opacity of the cloud (in cm^{-1}), and j_ν denotes its volume emissivity (in $\text{erg s}^{-1} \text{ cm}^{-3} \text{ Hz}^{-1}$). Eq (1) implicitly assumes that the cloud is static. To account for gas motion, we would need to Doppler boost into the frame of the gas at s . However, we will show in § 5 that the fine structure cross-sections are extremely broad in frequency, and that this Doppler boost can be safely ignored. For the relevant results in this paper, the second term on the right-hand-side of Eq (1) is much smaller than I_ν (see Appendix A) in which case Eq 1 simplifies to

$$I_\nu(s) = I_{\nu,0} e^{-\kappa_\nu s}. \quad (2)$$

The opacity through any transition is given by (see e.g. Rybicki & Lightman 1979, Eq 1.78)

$$\kappa_\nu = \kappa(\nu) = \frac{h\nu_{ul} B_{ul}}{4\pi \Delta\nu_{ul}} \times \left(\frac{g_u}{g_l} n_l - n_u \right) \phi(\nu), \quad (3)$$

$$j_\nu = j(\nu) = \frac{h\nu_{ul}}{4\pi \Delta\nu_{ul}} n_u A_{ul} \phi(\nu),$$

where $B_{ul} = \frac{c^2}{2h\nu^3} A_{ul}$, A_{ul} denotes the Einstein A-coefficient for the transition from the higher energy state ‘u’ to the lower energy state ‘l’. The energy difference

between the two states is given by $\Delta E = h\nu_{ul}$. The factors g_l and n_l (g_u and n_u) denote the statistical weight and number density of atoms in the lower (upper) energy state. The function $\phi(\nu)$ denotes the line profile function (also known as the Voigt function), which is normalized to unity through $\frac{1}{\Delta\nu_{ul}} \int d\nu \phi(\nu) = 1$, in which $\Delta\nu_{ul} \equiv \nu_{ul} \sqrt{\frac{2kT}{m_p c^2}}$.

We consider the $2p_{1/2} \rightarrow 2s_{1/2}$ (for which $g_l = 2$, $g_u = 2$, $A_{ul} = 1.60 \times 10^{-9} \text{ s}^{-1}$) and the $2s_{1/2} \rightarrow 2p_{3/2}$ transition (for which $g_l = 2$, $g_u = 4$, $A_{ul} = 8.78 \times 10^{-7} \text{ s}^{-1}$). We assume that the atoms in the $2p$ state are divided between $2p_{1/2}$ and $2p_{3/2}$ following their statistical weight. That is, for the 9.9 GHz transition we have $n_l = n_{2s}$ and $n_u = n_{2p} \times 2/3$, while for the 1.1 GHz we have $n_l = n_{2p} \times 1/3$ and $n_u = n_{2s}$. We justify adopting this assumption in § 5.

We write the line center total optical depth τ_0^{FS} through the center of the collapsing gas cloud of radius R_{cl} —in *both* fine structure transitions—as

$$\tau_0^{\text{FS}} \equiv 2R_{\text{cl}} \kappa_0 = R_{\text{cl}} \frac{\lambda^2 A_{ul}}{\pi} \times \left(\frac{g_u}{g_l} n_l - n_u \right) \frac{1}{A_\alpha}, \quad (4)$$

where $A_\alpha = 6.25 \times 10^8 \text{ s}^{-1}$ is the Einstein coefficient for the $2p \rightarrow 1s$ transition. This expression does not contain the temperature-dependent width $\Delta\nu_D$, because the Voigt parameter⁴ that is present in the Voigt

⁴ Both fine structure transitions involve transitions between 2s

function, $\phi(\nu)$ is $a_v = \frac{A_\alpha}{4\pi\Delta\nu_D} \approx 117(T_{\text{gas}}/10^4)^{-1/2}$ for the 3cm-transition, and $a_v \approx 13(T_{\text{gas}}/10^4)^{-1/2}$ for the 27cm-transition (Dijkstra et al. 2008b). The line profile function evaluated at line center is (see e.g. Chluba & Sunyaev 2009)

$$\phi(0) = \frac{1}{\sqrt{\pi}} \exp(a_v^2) \text{erfc}(a_v) \approx \frac{1}{\pi a_v} = \frac{4\Delta\nu_{\text{ul}}}{A_\alpha}, \quad (5)$$

where we have used that $\text{erfc}(a_v) \rightarrow \frac{e^{-a_v^2}}{a_v\sqrt{\pi}}$ when $a_v \gg 1$. The factor $\Delta\nu_{\text{ul}}$ that enters $\phi(0)$ cancels the one that is present in the expression for $j(\nu)$. The opacity through the fine structure transitions is therefore independent of temperature, which is because the fine structure transitions have large intrinsic spectral width (see Fig 6) and thermal broadening has no impact.

2.3. The Level Populations of HI

2.3.1. The 2s-Level

We first list the processes that populate the 2s-level, and quantify the rates at which these occur. We then list the processes that *de*-populate the 2s level. The processes that populate the 2s level include

- **Collisional excitation from the ground state.**

The total rate at which collisional excitation of a hydrogen atom in the ground state with a free electron leaves the hydrogen atomic its 2s state is $n_e n_{1s} C_{1s2s}$ (in $\text{cm}^{-3} \text{s}^{-1}$), where n_e denotes the number density of free electrons, and where

$$C_{1u} = 8.63 \times 10^{-6} T^{-1/2} \langle \Omega_{lu} \rangle \exp\left(-\frac{\Delta E_{lu}}{k_B T}\right) \text{cm}^3 \text{s}^{-1}. \quad (6)$$

Here, $\langle \Omega_{lu} \rangle$ denotes the ‘velocity averaged collision strength’ of the 1s-2s transition. We adopt $\langle \Omega_{lu} \rangle = 0.27$, which corresponds to the value appropriate at $T = 10^4 \text{ K}$ (with a very weak temperature dependence, see Scholz et al. 1990).

- **Indirect photo excitation by higher Lyman-series photons.**

The rate at which the 2s level is populated as a result of absorption of a Lyman series photon by HI in its ground state, which subsequently radiatively cascades down to the 2s state is $\Gamma_{\text{Ly}\alpha} n_{1s} P_{np2s}$ (in $\text{cm}^{-3} \text{s}^{-1}$). We can safely ignore this term in the gas clouds we are considering. This is because higher order Lyman series photons scatter only a small number of times before being converted into lower energies photons, with suppresses their scattering rate relative to that of $\text{Ly}\alpha$ by orders of magnitude (see Dijkstra et al. 2008b for an extended discussion).

- **Recombination into the 2s-state.**

The rate at which the 2s level is populated as a result of recombination of an electron and proton into the 2s state (either and 2p states, both of which have finite lifetimes. Under these conditions, the relevant Voigt parameter equals $a_v = \frac{A_\alpha + A_{2s1s}}{4\pi\Delta\nu_D}$, where $\Delta\nu_D = \frac{\nu_{\text{ul}}}{c} \sqrt{\frac{2kT}{m_p}}$ (see Eq 10.74, Rybicki & Lightman 1979). Since $A_\alpha \gg A_{2s1s}$, we have $a_v = \frac{A_\alpha}{4\pi\Delta\nu_D}$ to high accuracy.

through direct recombination into the 2s state, or via some intermediate higher energy state followed by a radiative cascade into 2s, is $\alpha_{2s} n_e n_p$ (in $\text{cm}^{-3} \text{s}^{-1}$). For case-B recombination, $f_{2s} \sim 32\%$ of all recombination events will result in an atom populating the 2s term (Spitzer & Greenstein 1951; Dennison et al. 2005). That is, $\alpha_{2s} = f_{2s} \alpha_{\text{rec,B}}$, where α_B denotes the case-B recombination coefficient, which we take from Hui & Gnedin (1997).

- **Collisional transitions 2p → 2s.** The 2s level can be populated as a result of a collisions between hydrogen atoms in their 2p with a free proton (collisions with electrons are ~ 10 times less efficient). The rate for this process is $n_p n_{2p} C_{2p2s}$ (in $\text{cm}^{-3} \text{s}^{-1}$), with the rate coefficient $C_{2p2s} = 1.8 \times 10^{-4} \text{ cm}^3 \text{ s}^{-1}$ (e.g. Dennison et al. 2005, and references therein).

- **Direct Radiative transitions 2p → 2s.** Finally, the 2s can be populated via direct radiative transitions, either via spontaneous or via CMB-induced transitions. This rate is $n_{2p}(A_{2p2s} + \Gamma_{2p2s}^{\text{CMB}})$. Spontaneous radiative transitions are only allowed for $2p_{3/2} \rightarrow 2s_{1/2}$, for which $A_{2p2s} = 8.78 \times 10^{-8} \text{ s}^{-1}$. Under our assumption that 2/3 of all atoms in 2p-state are in the $2p_{3/2}$ level (which we justify in § 5), this rate becomes $\frac{2}{3} n_{2p} A_{2p2s}$. The CMB induces transitions $2p \rightarrow 2s$ in two ways: (i) stimulated emission from the $2p_{3/2}$ state, and (ii) absorption from the $2p_{1/2}$ state. The rate at which this happens is $\frac{2}{3} n_{2p} \Gamma_{2p_{3/2}2s}^{\text{CMB}} + \frac{1}{3} n_{2p} \Gamma_{2p_{1/2}2s}^{\text{CMB}}$. This can be recast⁵ as $\frac{2}{3} n_{2p} \frac{1}{2} \Gamma_{2s2p_{3/2}}^{\text{CMB}} + \frac{1}{3} n_{2p} \Gamma_{2s2p_{1/2}}^{\text{CMB}} = \frac{1}{3} n_{2p} 9.3 \times 10^{-6} (1+z)$, where we adopted the rates from Eq A3 in Hirata (2006). In short, we define $\Gamma_{2p2s}^{\text{CMB}} \equiv 3.1 \times 10^{-6} (1+z) \text{ s}^{-1}$. It is also clear the CMB induced transitions dominate over spontaneous transitions.

Processes that *de*populate the 2s-level include

- **Collisional transitions 2s → 2p.** The rate at which HI atoms leave the 2s as a result of collisionally induced transitions to the 2p state is $C_{2s2p} n_p n_{2s}$ (in $\text{cm}^3 \text{ s}^{-1}$), where $C_{2s2p} = 3 \times C_{2p2s} = 5.3 \times 10^{-4} \text{ cm}^3 \text{ s}^{-1}$.

- **Two-photon Decay 2s → 1s.** The rate at which hydrogen atoms leave the 2s state as a result of a direct radiative transition to the ground state (by emitting two photons) is $n_{2s} A_{2s1s}$ (in $\text{cm}^3 \text{ s}^{-1}$). The Einstein A-coefficient for such a transition is $A_{2s1s} = 8.25 \text{ s}^{-1}$.

- **Direct Radiative transitions 2s → 2p.** Finally, the 2s can be depopulated via the direct radiative transitions mentioned above. This rate is $n_{2s}(A_{2s2p} + \Gamma_{2s2p}^{\text{CMB}})$.

⁵ Eq (4) shows that the cross-section for absorption from some lower state ‘l’ to an upper state ‘u’ equals the cross-section for stimulated emission from the upper to the lower level, but multiplied by the ratio of statistical weights $\frac{g_u}{g_l}$. The stimulated emission rate (per atom in the $2p_{3/2}$ state) from $2p_{3/2} \rightarrow 2s_{1/2}$ is therefore half that of the absorption rate (per atom in the $2s_{1/2}$ state) from $2s_{1/2} \rightarrow 2p_{3/2}$.

Spontaneous radiative transitions are only allowed for $2s_{1/2} \rightarrow 2p_{1/2}$, for which $A_{2s2p} = 1.60 \times 10^{-9} \text{ s}^{-1}$. The CMB again induces transitions $2s \rightarrow 2p$ in two ways: (i) stimulated emission from the $2s_{1/2}$ state, and (ii) absorption into the $2p_{3/2}$ state. Following the arguments given above, we can write the rate at which this happens as $n_{2s} \Gamma_{2s_{1/2}2p_{1/2}}^{\text{CMB}} + n_{2s} \Gamma_{2s_{1/2}2p_{3/2}}^{\text{CMB}} \equiv \Gamma_{2s2p}^{\text{CMB}} n_{2s}$. We note that $\Gamma_{2s2p}^{\text{CMB}} = 3\Gamma_{2p2s}^{\text{CMB}}$.

The equilibrium solution is given by

$$A + Bn_{2p} = Cn_{2s}, \quad (7)$$

with

$$\begin{aligned} A &= n_{1s} [n_e C_{1s2s} + \Gamma_{\text{Lyn}} P_{np2s}] + \alpha_{2s} n_e n_p, \quad (8) \\ B &= n_p C_{2p2s} + A_{2p2s} + \Gamma_{2p2s}^{\text{CMB}}, \\ C &= A_{2s1s} + A_{2s2p} + C_{2s2p} n_p + \Gamma_{2s2p}^{\text{CMB}}. \end{aligned}$$

2.3.2. The 2p-Level

The equilibrium solution of the 2p state can be written in a simplified form very similar to Eq 7:

$$D + En_{2s} = Fn_{2p}, \quad (9)$$

where

$$\begin{aligned} D &= n_{1s} \Gamma_\alpha \quad (10) \\ E &= n_p C_{2s2p} + \Gamma_{2s2p}^{\text{CMB}} \\ F &= A_\alpha + C_{2p2s} n_p + A_{2p2s} + \Gamma_{2p2s}^{\text{CMB}}. \end{aligned}$$

The structure of these terms is similar to those describing the population and depopulation of the 2s levels. The most significant difference is in the D -term, which only contains the term $\Gamma_\alpha n_{1s}$. This term denotes the rate at which Ly α photons are absorbed, i.e. scattered, by hydrogen atoms in the ground state into the 2p state. Because of the large optical depth of the gas cloud to Ly α photons, Ly α photons typically scatter many times off different atoms before escaping from the cloud. The Ly α scattering rate is therefore boosted compared to the Ly α production rate as

$$\begin{aligned} \Gamma_\alpha &= (\text{Ly}\alpha \text{ production rate per H atom}) \times \\ &\times (\text{number of scattering events per Ly}\alpha \text{ photon}) = \\ &= [n_e C_{1s2p} + \Gamma_{\text{Lyn}} P_{np2p} + \alpha_{2p} n_e n_p / n_{1s}] \langle N_{\text{scat}} \rangle \quad (11) \end{aligned}$$

where $\alpha_{2p} = f_{2p} \alpha_{\text{rec,B}}$ with $f_{2p} = 1 - f_{2s} \approx 0.68$ (see Dijkstra 2014, for a derivation), and where we adopt $\langle \Omega_{1s2p} \rangle = 0.47$ in the expression for C_{1s2p} (Scholz et al. 1990). Finally, $\langle N_{\text{scat}} \rangle$ denotes the mean number of times a Ly α photon scatters before it escapes from the cloud.

The Ly α scattering process can be described by diffusion in both real and frequency space (e.g. Adams 1972; Harrington 1973; Neufeld 1990). The diffusion in frequency space, combined with the strong frequency dependence of the Ly α absorption cross-section, causes $\langle N_{\text{scat}} \rangle$ to scale with the line center optical depth of

the medium to Ly α photons as $\langle N_{\text{scat}} \rangle \propto \tau_{\text{Ly}\alpha,0}$ (Adams 1972, as opposed to the $\langle N_{\text{scat}} \rangle \propto \tau^2$ dependence that is expected for a random walk in real space only). For Ly α photons emitted in the center of a uniform, static sphere we have $\langle N_{\text{scat}} \rangle \approx k_1 \tau_0$ with $k_1 = 0.6$ (Dijkstra et al. 2006). In our case the gas cloud is collapsing and is therefore not static. However, the infall velocity is expected to be close to the circular velocity of the dark matter halo hosting the gas cloud, which is $v_{\text{circ}} \sim 10 \text{ km s}^{-1}$. This infall velocity is comparable to the thermal velocity of the gas, and gas motions do not modify our estimate at all (e.g. Spaans & Silk 2006, and see § 5 for a more quantitative discussion).

The line center optical depth $\tau_0 \propto N_{\text{HI}} = 2n_{\text{HI}} R_{\text{cl}} \propto n^{2/3} M^{1/3} \propto n^{2/3}$ at fixed M , and therefore increases as the cloud continues its collapse. Importantly, $\langle N_{\text{scat}} \rangle$ does not increase indefinitely with τ_0 for four main reasons (in Appendix F we discuss a few more reasons that are less important):

1. At increasingly high densities, collisional de-excitation from the 2p state becomes more probable, which would result in the destruction of the Ly α photon. The probability that this occurs at any scattering event is given by $p_{\text{dest}} = \frac{n_p C_{2p2s}}{n_p C_{2p2s} + A_\alpha}$. At a given number density n , we therefore expect Ly α photons not to scatter more than $\approx p_{\text{dest}}^{-1}$ times.
2. Gas clouds collapsing into a DCBH do contain small amounts of molecular hydrogen, with $f_{H_2} \equiv n_{H_2}/n_{\text{H}} \sim 3\text{--}5 \times 10^{-9}$ (e.g. Shang et al. 2010; Latif et al. 2015). Molecular hydrogen has two transitions that lie close to the Ly α resonance: (a) the $v = 1 - 2P(5)$ transition, which lies $\Delta v = 99 \text{ km s}^{-1}$ redward of the Ly α resonance, and (b) the $1 - 2R(6)$ transition which lies $\Delta v = 15 \text{ km s}^{-1}$ redward of the Ly α resonance. Vibrationally excited H_2 may therefore convert Ly α photons into photons in the H_2 Lyman bands (Neufeld 1990, and references therein), and thus effectively destroy Ly α . Neufeld (1990) provides an expression for the escape fraction of Ly α photons from a static slab whose line centre optical depth from slab centre to slab edge is τ_0 , which we denote with $f_{\text{esc}}^{H_2}(\tau_0)$. We reproduce the full expression for $f_{\text{esc}}^{H_2}(\tau_0)$ in Appendix E. We take the simple approach and assume that $\langle N_{\text{scat}} \rangle \rightarrow \langle N_{\text{scat}} \rangle \times f_{\text{esc}}^{H_2}(\tau_0)$, i.e. only those photons that escape contribute to the scattering rate. The contribution from photons that are destroyed by molecular hydrogen is ignored.
3. When a non-negligible fraction of hydrogen atoms is in the first excited state, Ly α photons can photoionize these excited atoms. The photoionisation cross-section from the $n = 2$ by Ly α photons is $\sigma_{\text{ion}}^{\text{Ly}\alpha} = 5.8 \times 10^{-19} \text{ cm}^2$ (e.g. Cox 2000, p 108). Because Ly α photons scatter so frequently, their total path through the cloud is increased by a factor of $B = (a_v \tau_0 / \sqrt{\pi})^{1/3} \approx 12 (N_{\text{HI}} / 10^{20} \text{ cm}^{-2})^{1/3} (T / 10^4 \text{ K})^{-1/3}$ (Adams 1975). The total optical depth for photoionisation from the $n = 2$ state that Ly α photons experience equals $\tau_{\text{ion}}^{\text{Ly}\alpha} = B [n_{2p} + n_{2s}] \sigma_{\text{ion}} R_{\text{cl}} \equiv B \tau_{\text{ion}}$.

We can substitute $\tau_0 = \langle N_{\text{scat}} \rangle / k_1$ into the expression for B , and get a maximum number of scattering events that a Ly α photon can undergo by setting $\left(\frac{a_\nu N_{\text{scat}}^{\gamma, \text{max}}}{\sqrt{\pi} k_1}\right)^{1/3} \equiv 1$. This translates to $N_{\text{scat}}^{\gamma, \text{max}} = \frac{\sqrt{\pi} k_1}{a_\nu \tau_{\text{ion}}^3}$. Because τ_{ion} depends on the number density of hydrogen atoms in the $2s$ and $2p$ states (which we are trying to solve for), this complicates the analysis slightly. We first ignore this process. After computing n_{2p} and n_{2s} , we will verify whether this assumption was justified.

4. Finally, Ly α photons are destroyed in the maser cycle itself (see Fig 1). This becomes important when the maser saturates. We do not include this effect in our calculations, because it would require us to simultaneously solve for the level populations, and the amplified CMB through the cloud. Instead, we verify whether ignoring this effect was justified in § 3.3.

We therefore compute $\langle N_{\text{scat}} \rangle$ as

$$\langle N_{\text{scat}} \rangle = \min \left(k_1 \tau_{\text{Ly}\alpha, 0} f_{\text{esc}}^{H2}, p_{\text{dest}}^{-1} \right). \quad (12)$$

2.3.3. Solving the Rate Equations

For a primordial gas cloud with uniform density, the number density of hydrogen nuclei (i.e. free protons plus neutral hydrogen atoms), n , equals

$$n = \frac{3(1 - Y_{\text{He}}) M_{\text{gas}}}{4\pi R_{\text{cl}}^3 m_{\text{p}}} \approx 100 \left(\frac{M_{\text{gas}}}{10^7 M_{\odot}} \right) \left(\frac{R_{\text{cl}}}{0.1 \text{ kpc}} \right)^{-3} \text{ cm}^{-3} \quad (13)$$

where $Y_{\text{He}} = 0.24$ denotes the primordial Helium mass fraction.

To determine the fraction of hydrogen atoms in the first excited state, we need the gas temperature, and we therefore need to specify heating mechanisms. We assume that the gas is heated by two different processes:

- **Gravitational Heating.** This corresponds to the heating associated with the contraction of the cloud, which converts gravitational binding energy into kinetic energy, which in turn is converted into heat (e.g. Haiman et al. 2000). The total gravitational heating rate is thus

$$\begin{aligned} H^{\text{grav}} &= \frac{dU_{\text{bind}}}{dt} = \frac{3GM_{\text{gas}}^2}{5R^2} \dot{R} \quad (14) \\ &\approx 1.7 \times 10^{38} \text{ erg/s} \left(\frac{M_{\text{gas}}}{10^7 M_{\odot}} \right)^2 \left(\frac{R}{100 \text{ pc}} \right)^{-2} \left(\frac{\dot{R}}{10 \text{ km/s}} \right), \\ &\approx 1.7 \times 10^{38} \text{ erg/s} \left(\frac{M_{\text{gas}}}{10^7 M_{\odot}} \right)^2 \left(\frac{n}{100 \text{ cm}^{-3}} \right)^{2/3} \left(\frac{\dot{R}}{10 \text{ km/s}} \right), \end{aligned}$$

where we used that $U_{\text{bind}} = -\frac{3GM_{\text{gas}}^2}{5R}$. We therefore assumed that the dark matter does not contribute to the gravitational potential, which is appropriate when the gas has collapsed to the high densities that we consider in this paper.

- **Radiative Heating.** In case the gas is collapsing onto an in-place DCBH (see § 2), the radiation from the accretion disk can photoionize the gas cloud. When the total (maximum) recombination rate of the cloud, $\dot{N}_{\text{rec}}^{\text{max}} = \alpha_{\text{B}} n^2 \frac{4}{3} \pi R_{\text{cl}}^3$, exceeds the rate at which the accretion disk produces ionising photons, \dot{N}_{ion} , then the accretion disk will not be able to fully ionise the gas cloud. In this case, the cloud consists of an HII region of radius R_{ion} , which is surrounded by neutral gas (which extends out to R_{cl}). X-ray photons emitted by the accretion disk can penetrate this neutral gas and heat it. For the production rate of ionising photons we assume the DCBH is accreting at Eddington luminosity and that its spectrum is identical to that of unobscured, radio-quiet quasars⁶. Under these assumptions, $\dot{N}_{\text{ion}} = 6.5 \times 10^{53} \left(\frac{M_{\text{BH}}}{10^6 M_{\odot}} \right) \text{ s}^{-1}$.

The total maximum recombination rate of a cloud is $\dot{N}_{\text{rec}}^{\text{max}} = \frac{4}{3} \pi R_{\text{cl}}^3 n^2 \alpha_{\text{B}}(T) = \frac{M_{\text{gas}} n \alpha_{\text{B}}(T)}{\mu m_{\text{p}}}$. We obtain the ‘critical’ density, n_{crit} , beyond which the gas cloud cannot be kept ionised by setting $\dot{N}_{\text{rec}}^{\text{max}} = \dot{N}_{\text{ion}}$. This critical density equals

$$\begin{aligned} n_{\text{crit}} &= \frac{\mu m_{\text{p}} \dot{N}_{\text{ion}}}{M_{\text{gas}} \alpha_{\text{B}}(T)} \quad (15) \\ &\approx 240 \left(\frac{M_{\text{BH}}}{10^6 M_{\odot}} \right) \left(\frac{M_{\text{gas}}}{10^7 M_{\odot}} \right)^{-1} \left(\frac{T}{10^4 \text{ K}} \right)^{0.7} \text{ cm}^{-3}, \end{aligned}$$

where the T -dependence is due to the recombination coefficient. For $n > n_{\text{crit}}$ the radiative heating is important. The total column density of HI through the cloud is

$$\begin{aligned} N_{\text{HI}} &= n^{2/3} \left(\frac{3M_{\text{gas}}}{4\pi\mu m_{\text{p}}} \right)^{1/3} \left[1 - \left(\frac{n_{\text{crit}}}{n} \right)^{1/3} \right] = \quad (16) \\ &= n R_{\text{cl}} \left[1 - \left(\frac{n_{\text{crit}}}{n} \right)^{1/3} \right]. \end{aligned}$$

We use this to compute $\tau_{\text{Ly}\alpha, 0}$ and hence $\langle N_{\text{scat}} \rangle$.

When the radiative heating is important, we assume that a fraction f_{heat} of the X-ray luminosity goes into heating. The total heating rate is then

$$\begin{aligned} H^{\gamma} &= f_{\text{heat}} f_{\text{X}} L_{\text{ed}} \quad (17) \\ &= 1.3 \times 10^{42} \left(\frac{f_{\text{heat}}}{0.1} \right) \left(\frac{f_{\text{X}}}{0.1} \right) \left(\frac{M_{\text{BH}}}{10^6 M_{\odot}} \right) \text{ erg s}^{-1}, \end{aligned}$$

where the choice $f_{\text{X}} \sim 10\%$ is based on observations of luminous quasars for which 10% of their total bolometric luminosity is in the 0.5-10 keV band (e.g. Marconi et al. 2004; Lusso et al. 2012). The choice $f_{\text{heat}} = 10\%$ is arbitrary, but reflects the possibility that not all X-ray photons are absorbed in the gas, and that not all their energy goes into heating of the gas.

⁶ More specifically, this assumes a broken power-law spectrum of the form $f_{\nu} \propto \nu^{-0.5}$ for $1050 \text{ \AA} < \lambda < 1450 \text{ \AA}$, and $f_{\nu} \propto \nu^{-1.5}$ for $\lambda < 1050 \text{ \AA}$ (Bolton et al. 2011).

For a given heating process and density, we compute the equilibrium temperature T_{eq} for which radiative cooling balances this heating, i.e.

$$H = C_{\text{tot}}(T_{\text{eq}}, x_e), \quad (18)$$

where $C_{\text{tot}}(T_{\text{eq}}, x_e)$ denotes the total cooling rate. For the gas-temperatures encountered in this paper ($T = [0.6 - 1.2] \times 10^4$ K, see Appendix B for details) cooling is completely dominated by collisional excitation of atomic hydrogen (see e.g. Fig 1 of Thoul & Weinberg 1995), but we have included other cooling processes as well. Eq (18) simultaneously gives us the ionised fraction $x_e \equiv \frac{n_e}{n} = \frac{n_p}{n}$ and T_{eq} .

At this point, for a given n and heating mechanism, we have $n_e = n_p$ and T . We can then solve for n_{2s} and n_{2p} by combining Eq (7) and Eq (9) to give

$$\begin{aligned} n_{2p} &= \frac{CD + EA}{CF - EB}, \\ n_{2s} &= \frac{A + Bn_{2p}}{C}. \end{aligned} \quad (19)$$

where A, \dots, F were defined in Eq (11) and Eq (9).

After we have computed n_{2s} and n_{2p} , we verify whether $N_{\text{scat}}^{\gamma, \text{max}} > \langle N_{\text{scat}} \rangle$, where $N_{\text{scat}}^{\gamma, \text{max}}$ is the maximum number of scattering events a Ly α photon undergoes before photoionizing a hydrogen atom from its $n = 2$ state. If $N_{\text{scat}}^{\gamma, \text{max}} > \langle N_{\text{scat}} \rangle$ then our calculation is accurate. If on the other hand, $N_{\text{scat}}^{\gamma, \text{max}} < \langle N_{\text{scat}} \rangle$, then we allowed Ly α photons to scatter too frequently. As we show below, the number densities n_{2s} and n_{2p} both depend linearly on $\langle N_{\text{scat}} \rangle$. If we force $\langle N_{\text{scat}} \rangle$ - and therefore n_{2s} and n_{2p} - to be suppressed by a factor of x ($x < 1$), then $N_{\text{scat}}^{\gamma, \text{max}} \propto \tau_{\text{ion}}^{-3} \propto (n_{2p} + n_{2s})^{-3} \propto x^{-3}$. In this case, we want to increase $N_{\text{scat}}^{\gamma, \text{max}}$ such that it equals $\langle N_{\text{scat}} \rangle$. We achieve this by choosing $x = (N_{\text{scat}}^{\gamma, \text{max}} / \langle N_{\text{scat}} \rangle)^{1/3}$, and rescale $n_{2p} \rightarrow xn_{2p}$. We then recompute n_{2s} by applying Eq 19. We found that this correction is only necessary over a restricted range of densities, and that even it only corrects our predicted optical depths at the tens of per cent level.

3. RESULTS

3.1. The Number Densities n_{2s} and n_{2p}

Figure 2 shows both n_{2s} (solid lines) and n_{2p} (dotted lines) as a function of n for the case of gravitational heating (red lines), and radiative heating (black lines). The bottom-panel shows the density dependence of the slope $d \log n_{2s/2p} / d \log n$ of each of the lines shown in the top panel. The density-dependence of n_{2s} and n_{2p} is easy to understand. We discuss both separately:

- **2s-Level.** The lower red solid line that represents the gravitational heating scenario shows that $n_{2s} \propto n^{1.67}$ up to $\log(n/\text{cm}^{-3}) \sim 4.5$. This is because at these densities the 2s state is populated primarily via collisional excitation from the ground state, and depopulated via

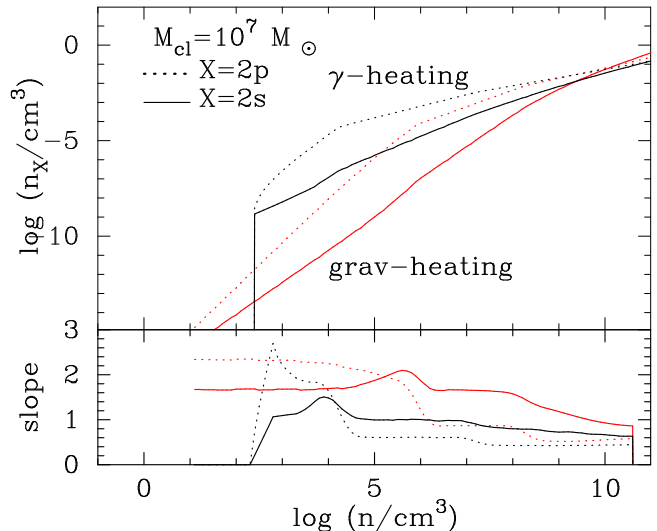


FIG. 2.— The top panel shows the dependence of n_{2s} (n_{2p}) on n as solid lines (dotted lines), for the cases of gravitational heating (red lines) and radiative heating (black lines). The lower panel shows the slope of these lines. Both n_{2p} and n_{2s} are $\ll n_{1s}$, i.e. atoms in the first excited state account for only a tiny fraction of hydrogen. The 2p-state is overpopulated with respect to the 2s-state at all densities, for both heating mechanisms in spite of the much shorter life-time of atoms in the 2p state. The reason the 2p-level is overpopulated is that Ly α scattering boosts the excitation rate into the 2p-state enormously. This overpopulation of the 2p-level leads to stimulated emission of the $2p_{3/2} \rightarrow 2s_{1/2}$ transition at $\lambda = 3$ cm. The number densities go to zero at $n \lesssim 240$ cm^{-3} in the radiative heating case as we expect the gas cloud to be fully ionised below these densities (see text).

two-photon emission, and thus $n_{2s} \propto n_e n_{1s} / A_{2s1s}$. Gas cooling is dominated by collisional excitation of atomic hydrogen, and the total cooling rate therefore scales as $L_{\text{cool}} \propto V n_e n_{1s}$, where V denotes the total volume of the cloud. The cooling rate balances the total gravitational heating rate, $H^{\text{grav}} \propto n^{2/3}$. We therefore can see that $n_e n_{1s} \propto L_{\text{cool}} / V = H^{\text{grav}} / V \propto n^{5/3}$, which explains the slope of the n_{2s} - n relation in Figure 2.

For intermediate density ($\log(n/\text{cm}^{-3}) \sim 4.5$ – 6.0) Figure 2 shows a steepening of the relation, which is because here the 2s level is populated via collisionally induced transitions $2p \rightarrow 2s$. The coupling to the 2p level boosts the density dependence of n_{2s} , because of the stronger density-dependence of n_{2p} at these densities (as shown by the dotted lines, we explain this density-dependence below).

At higher densities ($\log(n/\text{cm}^{-3}) \gtrsim 6.0$) Figure 2 shows that the slope of the n_{2s} - n relation is almost the same as in the low-density regime. The 2s-level is still populated primarily via collisional induced $2p \rightarrow 2s$ transitions, which locks the n_{2s} evolution to n_{2p} . However, at $\log n \gtrsim 6.0$ collisional destruction of Ly α photons becomes important which changes the density-dependence of n_{2p} . Finally, at very high densities the n_{2s} is limited by collisionally induced transitions of the form $2s \rightarrow 2p$.

The upper solid line represents the radiative heating scenario. The density-dependence of this curve can be understood in a similar way. The two main differences are that (i) for $n < n_{\text{crit}} \sim 240$ cm^{-3} (see Eq 16) the

cloud is fully ionised and $n_{2s} \sim 0$, and (ii) the total radiative heating rate H^γ does not depend on density, which causes $n_e n_{1s} \propto L_{\text{cool}}/V = H^\gamma/V \propto n$. This explains why the slope of the $n_{2s}-n$ line is flatter. The spike in the slope near $n \sim 240 \text{ cm}^{-3}$ is numerical. Finally, the enhanced number density of protons makes collisional deexcitation more important at lower densities in the radiative heating models, which is why the slope approaches $\sim 0.8-0.9$ at lower densities.

- **2p-Level.** Figure 2 also shows that the n -dependence of n_{2p} is different. We first discuss the gravitational heating scenario (the lines that represent the radiative heating models can be understood similarly). The $2p$ level is primarily populated via absorption of Ly α photons. The production of Ly α photons is dominated by collisional excitation. We showed in the discussion above that the collisional excitation rate increases as $n_e n_{1s} \propto n^{5/3}$. For low densities (now $\log n/(\text{cm}^{-3}) < 4.0$) the total average number of scattering events per Ly α photon increases as $\langle N_{\text{scat}} \rangle \propto \tau_0 \propto N_{\text{HI}} \propto n^{2/3}$. The total Ly α scattering rate therefore increases as $\propto n^{7/3}$, which is the density-dependence of n_{2p} shown in Figure 2.

At densities $\log n/(\text{cm}^{-3}) \sim 4.0-6.0$ the slope of the $n-n_{2p}$ flattens from $n_{2p} \propto n^{7/3}$ to $n_{2p} \propto n^{1.2}$ (with most change in the range $\log n \sim 5.0-6.0$). This change in the slope arises because $\langle N_{\text{scat}} \rangle$ becomes limited by H_2 , and $f_{\text{esc}}^{H_2}$ drops below unity for $\log n/(\text{cm}^{-3}) > 4.0$. At higher densities ($\log n/(\text{cm}^{-3}) \gtrsim 6.0$), collisional deexcitation becomes important, and we have $\langle N_{\text{scat}} \rangle \propto n_p^{-1}$. The proton number density n_p only increases $\propto n$ at fixed temperature. Because the cloud temperature (slightly) decreases with n , $n_p \propto n^{0.8}$ (see Fig 9 in Appendix B), and we have $n_{2p} \propto n^{5/3} \langle N_{\text{scat}} \rangle \propto n^{5/3} n_p^{-1} \propto n^{5/3-0.8} \propto n^{0.8-0.9}$, which is what is shown in Figure 2 up to $\log n/(\text{cm}^{-3}) \sim 8.0$. Finally, at the highest densities $\log n/(\text{cm}^{-3}) \gtrsim 8.0$, $n_{2p} \propto n^{0.5-0.6}$, which is because the number of times Ly α photons scatter ($\langle N_{\text{scat}} \rangle$) is limited by the optical depth to photoionisation from the $n = 2$ state (see Fig 10 in Appendix B). In this case $n_{2p} \propto N_{\text{scat}}^{\text{max}} n^{5/3} \propto \tau_{\text{ion}}^{-3} n^{5/3} \propto n_{2p}^{-3} n^{5/3}$, which therefore implies that $n_{2p}^4 \propto n^{5/3}$, i.e. $n_{2p} \propto n^{5/12} \approx n^{0.4}$, which is close to what we see.

Initially, the $2p$ state is significantly overpopulated relative to the $2s$ state. The simplest explanation for this is that the $2p$ population rate is boosted by $\langle N_{\text{scat}} \rangle$ compared to $2s$ -population rate. This boost $\langle N_{\text{scat}} \rangle$ lies in the range $\log \langle N_{\text{scat}} \rangle \sim 8-11$ (see Fig 10 in Appendix B), and overcompensates for the enormously shorter natural lifetimes of the $2p$ state ($t = A_\alpha^{-1} \sim 10^{-9}$ s) compared to the $2s$ state ($t = A_{2s1s}^{-1} \sim 0.1$ s). The weaker n -dependence of $2p$ at high densities, allows the $2s$ population to ‘catch-up’. At the highest densities we find that $n_{2p}/n_{2s} \sim 0.6$ for gravitational heating, and $n_{2p}/n_{2s} \sim 2.6$ for radiative heating. Note that with $n \rightarrow \infty$ we expect that $n_{2p}/n_{2s} \rightarrow C_{2s2p}/C_{2p2s} = 3$. This limit is not reached yet because the $2p$ -level is still predominantly populated via Ly α absorption, which elevates n_{2p} above the value

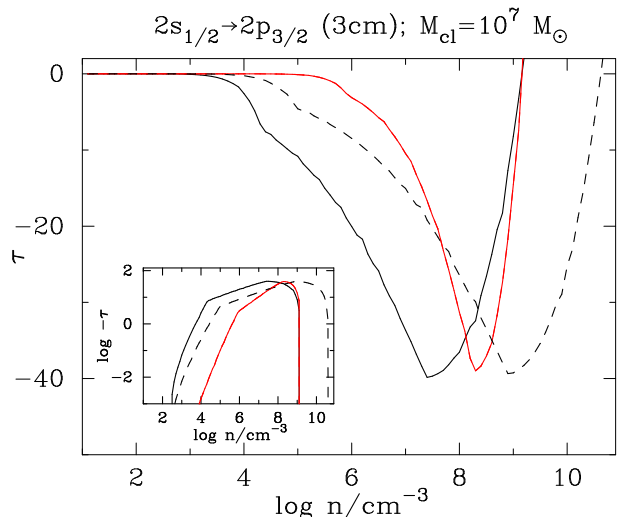


FIG. 3.— The optical depth τ_0 through the centre of the cloud (total mass $10^7 M_\odot$) in the 3-cm ($2s_{1/2} \rightarrow 2p_{3/2}$) fine-structure transition for the case of gravitational heating (red solid line), and radiative heating with $H^\gamma = 10^{43} \text{ erg s}^{-1}$ (black solid line) and $H^\gamma = 10^{42} \text{ erg s}^{-1}$ (black dashed line). The enhanced population in the $2p$ -state (see Fig 2) gives rise to considerable negative optical depth. The gas cloud thus acts as a maser amplifying the background CMB. The total amplification depends little on the precise heating mechanism, though this mechanism does determine at what density the maximum amplification is reached (see text for a quantitative analysis of all these plots).

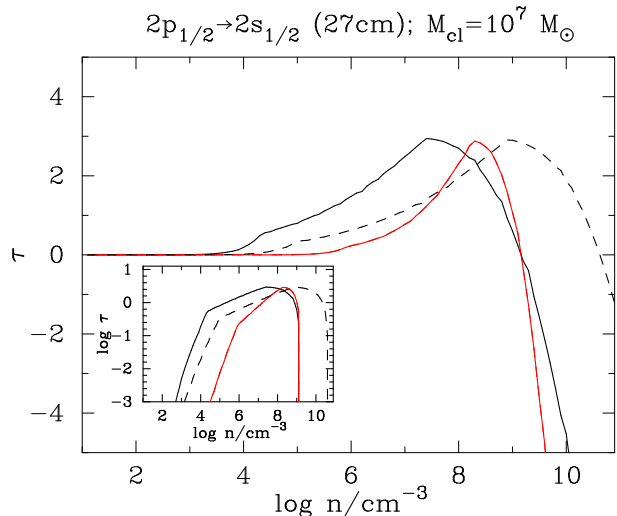


FIG. 4.— Same as Fig 3, but for the 27-cm ($2p_{1/2} \rightarrow 2s_{1/2}$) fine-structure transition. The precise density dependence of the optical depth closely follows that of the optical depth through the 3-cm transition, but with the sign reversed and its amplitude suppressed. At very high densities $\log n/(\text{cm}^{-3}) \gtrsim 9$ we get strong stimulated emission where $\tau_0 \propto -n_{2s} R_{\text{cl}} \propto -n^{0.5-0.6}$.

expected for thermal equilibrium.

3.2. The Line Center Optical Depth τ_0^{FS}

Using the values of n_{2s} and n_{2p} at a given n and T , we use Eq 4 to compute τ_0 in both fine structure transitions. Figure 3 shows τ_0 for the 3-cm ($2s_{1/2} \rightarrow 2p_{3/2}$ transition), and Figure 4 shows τ_0 for the 27-cm ($2p_{1/2} \rightarrow 2s_{1/2}$) transition. The solid red lines show the case of

gravitational heating, while the *black solid (black dashed lines)* show cases for radiative heating with $H^\gamma = 10^{43}$ erg s^{-1} ($H^\gamma = 10^{42}$ erg s^{-1}). These figures show that

- the optical depth through the 3-cm transition is negative, which is expected given the overpopulation of the $2p$ -level as compared to the $2s$ level.
- the optical depth through the 3-cm transition is significant irrespective of the heating mechanism: for each model the optical depth reaches⁷ $\tau_0 \sim -40$. The precise heating mechanism only affects the density at which the optical depth reaches its minimum. For low n , we have a significant over-population of atoms in the $2p$ -level, and $|\tau_0| \propto R_{\text{cl}} n_{2p} \propto n^{-1/3+7/3} \propto n^2$. The gravitational heating model indeed shows this behaviour in the low-density regime (with $\log n/(\text{cm}^{-3}) < 6.0$). At higher densities, Eq 4 shows that the optical depth changes sign when $n_{2p} = 3n_{2s}$ which occurs at $\log n/(\text{cm}^{-3}) \sim 9$. The radiative heating model with $H^\gamma = 10^{43}$ erg s^{-1} (*black solid line*) behaves very similar, but shifted towards lower densities. The model with an order of magnitude less radiative heating (*black dashed line*) is shifted back to higher densities again.
- the optical depth through the 27-cm transition is positive, and significantly smaller than that in the (absolute value of the) 3-cm transition. The main reason for this is that A_{ul} is smaller by a factor ~ 550 . The precise density dependence closely follows that of the optical depth through the 3-cm transition, and becomes negative when $n_{2p} = 3n_{2s}$. At very high densities $\log n/(\text{cm}^{-3}) \gtrsim 9$ we get strong stimulated emission where $|\tau_0| \propto n_{2s} R_{\text{cl}} \propto n^{0.5-0.6}$.

3.3. The 3.04-cm Signal

Eq 2 shows that $I_\nu(s) = I_{\nu,0} e^{-\tau_0^{\text{FS}}}$. The incoming radiation field is that of the CMB. We first recast this expression in terms of the brightness temperature, and compute the brightness temperature difference with the CMB. For $\tau_0^{\text{FS}} < 0$, the brightness temperature is enhanced exponentially:

$$\Delta T_b(\nu) = T_{\text{CMB}} (\exp [|\tau^{\text{FS}}(\nu)|] - 1), \quad (20)$$

where we have introduced the frequency dependence by replacing $\tau_0^{\text{FS}} \rightarrow \tau^{\text{FS}}(\nu)$ (details follow below). The exponential enhancement of the brightness temperature cannot take on arbitrarily large values as the amplified CMB inside the cloud affects the $2p$ and $2s$ level

⁷ A quick check of this result can be obtained from results reported in the literature. Field & Partridge (1961) find that $\tau_0(\text{H}\alpha) \approx -700\tau_0(3\text{cm})$ (for gas at $T = 5000$ K). The line centre cross-section for $\text{H}\alpha$ is $\sigma_{\text{H}\alpha,0} \sim 5 \times 10^{-13} (T/10^4 \text{ K})^{-1/2}$, and therefore $\sigma_{3\text{cm},0} = 7 \times 10^{-16} \text{ cm}^2$. Figure 3 shows that the minimum for $\tau_{3\text{cm}}$ is reached for $\log n/(\text{cm}^{-3}) \sim 9.0$ for gravitational heating, for which $n_{2p} \sim 10^{-2} \text{ cm}^{-3}$ and $R_{\text{cl}} \sim 0.5 \text{ pc}$. We therefore have $\tau_{3\text{cm}} \sim 2R_{\text{cl}} n_{2p} \sigma_{3\text{cm},0} \sim -30$. This estimate is a factor of ~ 1.5 lower than our full calculations (though clearly in the same ballpark). Appendix D discusses this in more detail.

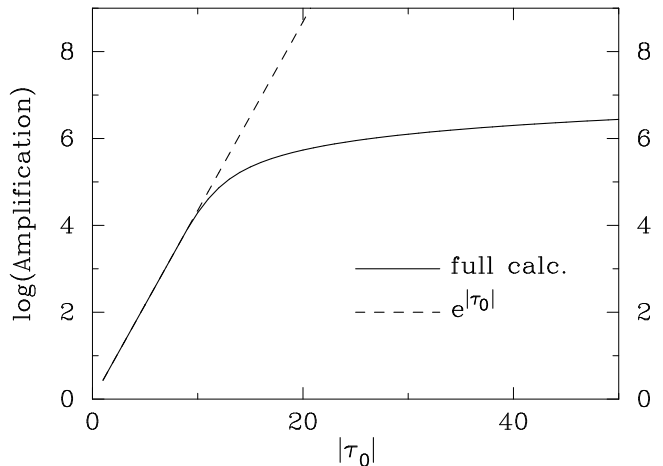


FIG. 5.— This Figure shows that maser amplification factor as a function of τ_0 . The *dashed line* shows amplification by a factor of $e^{|\tau_0|}$, while the *solid line* shows the actual amplification factor. For $\tau_0 \gtrsim 10$, the amplified CMB field affects the $2s$ and $2p$ level population, which causes the maser to saturate at amplification factors above $\sim 10^5$.

populations, which saturates the maser. The radiative transitions induced by the CMB occur at a rate $\Gamma_{2p2s}^{\text{CMB}} \equiv 3.1 \times 10^{-6} (1+z) = 3.4 \times 10^{-5} \text{ s}^{-1}$. We have repeated our analysis and amplified the CMB intensity by a factor of B_{CMB} and computed τ_0^{FS} as a function of B_{CMB} (at fixed n). Results of this calculation (shown in Appendix C) show that the maser starts to “shut off” when $B_{\text{CMB}} \gtrsim 10^5$. At this value of B_{CMB} the $2s$ -level is populated at a rate comparable to A_{2s1s} , and at larger values the $2s$ and $2p$ starts to approach the LTE value. The *solid line* in Figure 5 shows ΔT_b as a function of τ_0 , properly taking this effect into account. The *dashed line* shows $T_{\text{CMB}} \exp (|\tau^{\text{FS}}(\nu)|)$. This Figure illustrates the effect of maser saturation at $\tau_0 \gtrsim 10$, at an amplification factor $\gtrsim 10^5$.

Hyperfine splitting of the 3-cm line separates the $2p_{3/2} \rightarrow 2s_{1/2}$ transitions into three components at $\nu_1 = 9852$ MHz, $\nu_2 = 9876$ MHz, and $\nu_3 = 10030$ MHz, with line strength ratios 1:5:2 (Wild 1952; Ershov 1987; Dennison et al. 2005). Our previous calculations summed over all these transitions. However, these transitions are sufficiently separated in frequency that they can be resolved. We rewrite the expression for the brightness temperature contrast as

$$\Delta T_b(\nu) = T_{\text{CMB}} \left(\exp \left[\frac{|\tau_0^{\text{FS}}| \phi(\nu)}{\phi(\nu_{\text{FS}})} \right] - 1 \right), \quad (21)$$

where $\phi(\nu)$ is the 3-cm profile, and $\phi(\nu_{\text{FS}})$ denotes the fine structure line evaluated at line centre. To account for hyperfine splitting, we approximate $\phi(\nu)$ as the sum over 3 Voigt profiles

$$\phi(\nu) = \frac{1}{8} \phi_1(\nu) + \frac{5}{8} \phi_2(\nu) + \frac{2}{8} \phi_3(\nu), \quad (22)$$

where $\phi_n(\nu)$ denotes the Voigt profile of the n^{th} hyperfine transition. These profiles have the same spectral shapes, but are shifted in frequency.

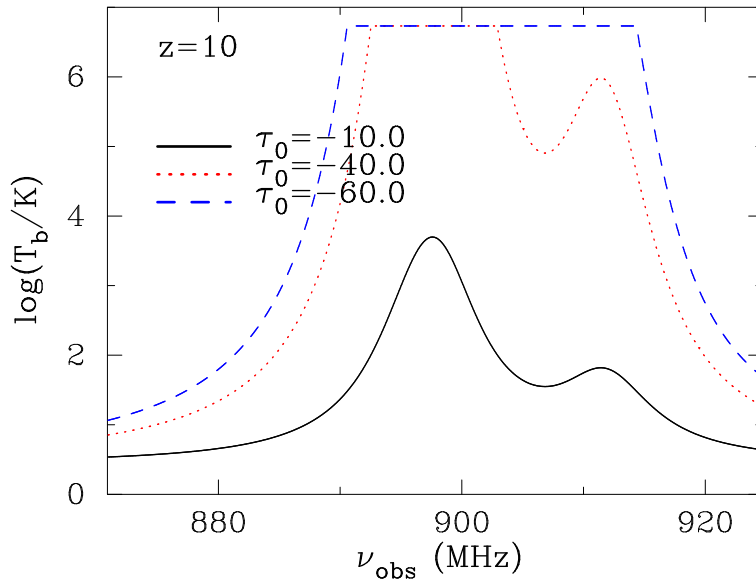


FIG. 6.— The brightness temperature contrast, $\Delta T_b(\nu)$, of the redshifted 3-cm transition of atomic hydrogen for three values of τ_0^{FS} as a function of observed frequency ν_{obs} in MHz. The inverted level populations of this transition give rise to stimulated emission that is orders of magnitude brighter than the CMB. The stimulated emission starts affecting the level populations for maser implication factors in excess $\sim 10^5$, and the maser saturates at $\Delta T_b(\nu) \gtrsim 10^{6-7}$ K. The features in the spectrum are due to hyperfine splitting in the 3-cm transition. In the $\tau_0^{\text{FS}} = -60$ case (the blue dashed line) maser saturation washes out this structure.

Figure 6 shows $\Delta T_b(\nu)$ as a function of ν for three different values of τ_0^{FS} . We have redshifted the profiles from $z = 10$ into the observers frame. Note that the only way redshift entered our calculations is through the CMB-induced transitions. This Figure shows how stimulated emission amplifies the CMB enormously. The black solid line shows $\Delta T_b(\nu)$ for $\tau_0 = -10$ which boosts the CMB by a factor of $e^{10} \sim 10^4$, and clearly shows the hyperfine structure of the 3-cm transition. The red dotted line corresponds to the case of $\tau_0^{\text{FS}} \sim -40$, which reaches a maximum at $\Delta T_b(\nu) \sim 10^7$ K. For larger τ_0 even the weaker hyperfine transition at $\nu_{\text{rest}} = 10030$ MHz is saturated, and the structure of the line is washed out (as illustrated by the blue dashed line).

The signal we computed is confined to a very small angular scale. The angular diameter of the cloud at $z = 10$ is

$$\theta_{\text{cl}} = \frac{2R_{\text{cl}}}{D_A(z)} = 1.2 \left(\frac{n}{10^6 \text{ cm}^{-3}} \right)^{-1/3} \left(\frac{M}{10^7 M_\odot} \right)^{1/3} \text{ mas}, \quad (23)$$

where $d_A(z)$ denotes the angular diameter distance to redshift z . Moreover, stimulated emission can be highly beamed (e.g. Goldreich & Keeley 1972; Alcock & Ross 1985a; Elitzur 1990a), which would further reduce the angular extend of the high brightness temperature source. This beaming depends on the degree of saturation of the gas cloud: gas on the edge of a spherical cloud that amplifies radiation in a uniform and isotropic background (as is the case here), sees maximally amplified radiation coming from the opposite side of the cloud. Similarly, gas in the center of the cloud sees the lowest level of amplification. There are three degrees of saturation, which relate to the extend of the ‘unsaturated core’ of the masing cloud (see Goldreich & Keeley 1972; Alcock & Ross 1985a,b; Elitzur 1990a,b).

- In *unsaturated* clouds, maser amplification is not saturated in any part of the cloud. In our case, this means that the $\tau_0^{\text{FS}} \lesssim 10$ (see Fig 5). For these clouds, the CMB is exponentially amplified along all paths through the cloud.
- In *partially saturated* clouds, the maser amplification is saturated outside a central region. In our case this translates to $10 \lesssim \tau_0^{\text{FS}} \lesssim 20$. The CMB is only amplified exponentially along paths that intersect the unsaturated core. The amplified CMB would point mostly radially outward outside the unsaturated core (e.g. Goldreich & Keeley 1972), in which case the angular extend of the cloud is more closely related to the size of the unsaturated core.
- In *full saturated* clouds, maser amplification is saturated everywhere. The angular size of the masing region is significantly smaller than the angular size of the cloud (Goldreich & Keeley 1972; Elitzur 1990a,b).

Angular sizes of spherical, partially and fully saturated masers have been calculated by Goldreich & Keeley (1972); Elitzur (1990a). Results of these calculations cannot be applied directly to our results because in the 3-cm both the life-time and pumping rates of both levels participating in the maser differ greatly, while Goldreich & Keeley (1972) assumed equal life-times for both levels. We will defer modifying their formalism to future work, and will only focus on the unsaturated regime. We will indicate where our calculations break down. The observed flux density of the signal at a (observed) frequency λ_0 is

$$F_\nu = \frac{2k_B}{\lambda_0^2 D_A^2(z)} \int_0^R 2\pi x dx \Delta T_b(\nu, x), \quad (24)$$

where x denotes the projected distance from the center of the cloud. For $z = 10$ we have $\lambda_0 \simeq 33$ cm. The

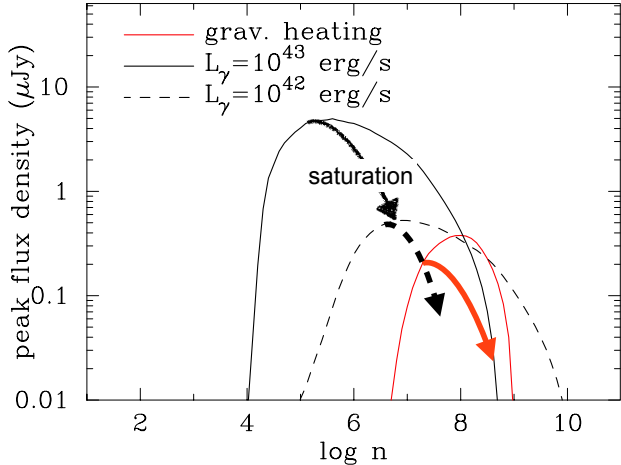


FIG. 7.— The predicted flux density (in μJy) in the 3-cm transition as a function of cloud density n , for the three models discussed in previous plots. This Figure shows that for gravitational heating only, we reach a maximum flux density $F_\nu \sim 0.5 \mu\text{Jy}$ for a narrow range of densities. This range is enhanced to $F_\nu \sim 5 \mu\text{Jy}$ for the radiative heating model with $H^\gamma = 10^{43} \text{ erg s}^{-1}$, and over a broader range of densities. These calculations assume that the masing cloud is unsaturated. This assumption breaks down at the densities that are indicated by the *thick arrows*, which indicate that the *thin lines* overpredict the flux densities. These predicted flux densities are within reach of surveys being planned with SKA1-MID (see text).

thin lines in Figure 7 shows the predicted flux density (in μJy) as a function of cloud density n for each of the three models shown previously (as given by Eq 24). Figure 7 shows that for the gravitational heating and radiative heating models with $H^\gamma = 10^{42} \text{ erg s}^{-1}$ the model flux density peaks at $F_\nu \sim 0.5 \mu\text{Jy}$ for a narrow range of densities. Radiative heating at $H^\gamma = 10^{43} \text{ erg s}^{-1}$ can boost the flux up to $F_\nu \sim 5 \mu\text{Jy}$. The *thicker lines with arrows* indicate the density at which the cloud becomes partially saturated, and that Eq 24 overestimates F_ν at larger densities.

Beaming is more pronounced in non-spherical masers. For flattened clouds, stimulated emission is highly beamed along longest axis of the cloud (see Goldreich & Keeley 1972; Alcock & Ross 1985a,b), and their apparent angular extend is more closely related to the physical area of the cloud perpendicular to this sightline. An additional complication to beaming through non-spherical clouds arises in the radiative heating models as these contain a central ionized bubble, which also affects the radiative transfer of stimulated emission. This effect is most important for the radiative heating model with $H^\gamma = 10^{43} \text{ erg s}^{-1}$, where the radius of the ionized bubble at the predicted peak flux density is $\sim 10\%$ of that of the cloud as a whole (see Eq 17). This effect is likely much less important than the effects of beaming. Future calculations should nevertheless consider the impact of the ionized bubble.

The predicted 3-cm flux peaks at the onset of maser saturation. Here, we verify whether we were justified to ignore destruction of $\text{Ly}\alpha$ photons in the maser cycle in our calculation of the $\text{Ly}\alpha$ pumping rate. We focus on the radiative heating model with $H^\gamma = 10^{43} \text{ erg s}^{-1}$, but note

that the same reasoning applies to the other models. The predicted flux density peaks at $\log[n/\text{cm}^{-3}] \sim 5$ for this model, at which $\tau_0^{\text{FS}} \sim 10$. Stimulated emission from the amplified CMB occurs at a rate $\frac{\Omega_{\text{Amp}}}{4\pi} \times \text{Amplification} \times \Gamma_{2p2s}^{\text{CMB}} \sim \frac{\Omega_{\text{Amp}}}{4\pi} \times 0.3([1+z]/11) \text{ s}^{-1}$ for the associated amplification of $\sim 10^4$ (see Fig 5). For the unsaturated case, most gas in the collapsing cloud sees a boost in the CMB well below this, as the maximum path length towards most gas is less than $\tau_0 \sim 10$. Only the gas on the edge of the cloud ‘sees’ the maximum amplification, and only from a solid angle $\Omega_{\text{Amp}} \ll 4\pi$. The destruction probability of a $\text{Ly}\alpha$ photon due to stimulated emission from the $2p$ state is the $P = \frac{\Omega_{\text{Amp}}}{4\pi} \times 5 \times 10^{-10}([1+z]/11)$, which limits the number of scattering events to $N_{\text{scat}} \sim 2 \times 10^9 \frac{4\pi}{\Omega_{\text{Amp}}} (11/[1+z])$, which is a factor $\sim 5 \frac{\Omega_{\text{Amp}}}{4\pi} ([1+z]/11)$ below the actual number of scattering events. Given that this correction only becomes relevant near the edge of the cloud, where $\Omega_{\text{Amp}} \ll 4\pi$ (and where therefore this correction is small anyway), our overall predicted flux is barely affected by $\text{Ly}\alpha$ destruction in the maser cycle, and confirms that this effect becomes important at the onset of maser saturation.

Finally, we point out that free-free opacity $\kappa(\nu) = 3.3 \times 10^{-7} n_e^2 T_{e,4}^{-1.35} (\nu/\text{GHz})^{-2.1} \text{ pc}^{-1}$ (Condon 1992) is clearly negligible inside the collapsing cloud (here, $T_{e,4}$ denotes the electron temperature in units of 10^4 K). In addition to this, the free-free opacity of the ionized IGM and our own Galaxy are negligible for $\nu \gtrsim 100 \text{ Mhz}$ (where ν denotes the frequency in the observer frame, see Spaans & Norman 1997), which corresponds to $z \lesssim 100$ for 3-cm masers. We discuss the detectability of this signal in § 4 below.

4. DETECTABILITY OF THE SIGNAL

The upcoming radio interferometer SKA will have the capability to detect the predicted signal. As a part of the Key Science Projects (KSP) with SKA1-MID (the first phase of SKA at medium frequencies: $0.4 \text{ GHz} < \nu < 20 \text{ GHz}$) thousands of hours of integration will be carried out in the frequency range of interest to us for line (redshifted HI) and continuum surveys, with ultra deep surveys using integration of over 1000 hours on a single pointing⁸. Such ultra-deep surveys might carry out up to 2 years of integration on multiple pointings. Planned continuum surveys with bandwidth $\Delta\nu = 0.3\nu$ will reach RMS noise of 100 nJy in 1000 hours at $\nu \simeq 900 \text{ MHz}$. Figure 6 shows the line width of the $2p$ - $2s$ signal $\delta\nu \simeq 10$ - 25 MHz . Assuming $\delta\nu = 10 \text{ MHz}$ gives an RMS of nearly 500 nJy at $\nu \simeq 900 \text{ MHz}$, which will allow for a significant detection for some of our models using SKA1-MID.

What is the expected number of observable $2p$ - $2s$ masers from $z \simeq 10$? The space density of DCBHs at $z \simeq 10$ is highly uncertain, and could lie in the range 10^{-3} - $10^{-10} \text{ cMpc}^{-3}$ (see e.g. Fig 4 of Dijkstra et al.

⁸ see e.g. <http://astronomers.skatelescope.org/wp-content/uploads/2015/08/SKA-SCI-LVL-001W.pdf>

2014). The comoving volume corresponding to a single SKA pointing (angular extent of nearly 1 square degree and bandwidth of 300 MHz for a central frequency $\simeq 900$ MHz) is $\simeq 2 \times 10^8 \text{ cMpc}^3$, covering a redshift range $8 < z < 12$. Even though a single pointing might contain a large number of DCBHs, observing their 3-cm fine structure transition is challenging, as they are observable only when they are emitting at peak flux, which occurs only for a limited range of densities.

5. DISCUSSION OF MODEL ASSUMPTIONS

1. The number density n_{2p} depends directly on $\langle N_{\text{scat}} \rangle$. We adopted $\langle N_{\text{scat}} \rangle = k_1 \tau_0$ which is strictly only valid for a static medium. The clouds we are interested in are collapsing, and we may therefore have overestimated $\langle N_{\text{scat}} \rangle$. The effect of ignoring the kinematics is not important. As we mentioned earlier, the collapse of the clouds occurs at velocities of order the circular velocity of the dark matter halo, i.e. $v \sim 10 \text{ km s}^{-1}$, which corresponds to the thermal width of the line profile. The velocity gradients through the clouds are therefore of order v/R_{cl} , and the Sobolev optical depth is $\tau \sim v_{\text{th}}/[v/R_{\text{cl}}] \sim R_{\text{cl}}$. In other words, velocity gradients only introduce a minor correction to the scattering rate⁹. It is also worth stressing that $\langle N_{\text{scat}} \rangle$ is limited in our model by collisional deexcitation and photoionisation from the $n = 2$ level, and as a result Ly α photons typically diffuse in real space by a fraction of the physical size of the cloud (also see discussion below).

Of course, given that $\Delta T_{\text{b}}(\nu)$ depends exponentially on $\langle N_{\text{scat}} \rangle$ it is worth studying this effect in more detail for more realistic models. One other aspect that can be addressed with more realistic models is that even though fragmentation is suppressed, density inhomogeneities can possibly give rise to lower column densities paths which allow Ly α photons to escape, and which can suppress $\langle N_{\text{scat}} \rangle$. These calculations are challenging as ordinary techniques that are used to perform Ly α radiative transfer simulations in simulations often speed-up the transfer problem by skipping the majority of scattering events.

2. Our adopted $\langle N_{\text{scat}} \rangle$ is appropriate for a static, spherical gas cloud. For flattened gas clouds, it is likely that Ly α photons escape in the direction of lowest N_{HI} , which can reduce $\langle N_{\text{scat}} \rangle$ at fixed n . However, Figure 10 in the Appendix shows clearly how for both the gravitational and radiative heating cases, $\langle N_{\text{scat}} \rangle$ is suppressed by $\sim 2 - 3$ orders of magnitude due to collisional deexcitation and photoionisation from the $n = 2$ level compared to calculations that ignore these

⁹ Bonilha et al. (1979) show that $\langle N_{\text{scat}} \rangle$ reduces to $\langle N_{\text{scat}}^{\text{vel}} \rangle$ by an amount $\frac{\langle N_{\text{scat}}^{\text{vel}} \rangle}{\langle N_{\text{scat}} \rangle} = \frac{1}{1+0.05\xi^{1.5}}$, where $\xi = \frac{1}{\sqrt{3}} B \frac{\Delta V}{x_{\text{peak}}}$, in which $B = (a_v \tau_0 / \sqrt{\pi})^{1/3}$ is the boost in path length that we introduced before (see § 2.3). ΔV denotes the difference in velocity between cloud edge and centre, and x_{peak} is the frequency at which Ly α photons are most likely to escape. For the column densities of interest, $x_{\text{peak}} > 10^3 \text{ km s}^{-1}$ (see Eq. in Dijkstra 2014), $B \sim 10^2$, and we get that ξ is of order unity. It is then clear that velocity gradients do not affect $\langle N_{\text{scat}} \rangle$ at all in our scenario.

processes. This suggests that each Ly α photon is effectively destroyed after it traversed a column density that is $\sim 2 - 3$ orders of magnitude smaller than the cloud column density (since $\langle N_{\text{scat}} \rangle \propto N_{\text{HI}}$). In other words, Ly α photons have only moved a fraction of the physical size of the cloud before being destroyed. This implies that $\langle N_{\text{scat}} \rangle$ depends weakly on the assumed spherical geometry.

3. We also ignore velocity structure in the cloud when we compute the maser amplification factor. This assumption is again safe. The profile of the fine structure lines are extremely broad (Wild 1952; Ershov 1987; Dennison et al. 2005). For example, the absorption line profile falls by a factor of 2 at nearly $\sim 10^3 \text{ km s}^{-1}$ away from line centre (and $\phi(\nu)$ drops only by 1% 100 km s^{-1} away from line center). Gas motions can therefore be safely ignored.
4. Throughout our analysis we always assumed that the $2p_{3/2}$ and $2p_{1/2}$ levels were populated according to their statistical weight, i.e. $n_{2p_{3/2}} = 2n_{2p_{1/2}}$. Both levels are populated by Ly α scattering. The frequency off-set between $2p_{3/2}$ and $2p_{1/2}$ is $\Delta\nu \sim 10^{10} \text{ Hz}$, which is $\sim 10\%$ of the thermal width of the Ly α line at $T \sim 10^4 \text{ K}$ (i.e. $\Delta\nu \sim 0.1\Delta\nu_{\text{D}}$). We expect the rate at which Ly α photons to populate the $2p_{3/2}$ and $2p_{1/2}$ levels to depend on the shape of the Ly α spectrum around these frequencies. In other words, we expect the rate at which the $2p_{3/2}$ and $2p_{1/2}$ are populated to depend on the color-temperature of the Ly α radiation field near the line resonance, which equals the gas temperature when gas is extremely opaque to Ly α radiation (Wouthuysen 1952; Field 1958). Because the mean thermal energy of the gas (kT) exceeds the energy difference between the $2p_{3/2}$ and $2p_{1/2}$ levels, we expect these two levels to be in statistical equilibrium.

6. CONCLUSIONS

The direct collapse black hole (DCBH) scenario describes the isothermal collapse of a pristine gas cloud directly into a massive, $M_{\text{BH}} = 10^4 - 10^6 M_{\odot}$ black hole. DCBH formation is a remarkably complex problem to tackle theoretically, and it would be extremely helpful to have observational diagnostics of this process.

In this paper, we have studied the detectability of the *fine structure* transitions of atomic hydrogen from gas clouds collapsing into or onto a DCBH. We have focussed on the strongest fine-structure transitions, namely the $2s_{1/2} - 2p_{3/2}$ transition with a rest frame wavelength of $\lambda = 3.04 \text{ cm}$, and the $2p_{1/2} - 2s_{1/2}$ transition at $\lambda = 27 \text{ cm}$. A detectable fine-structure signal from atomic hydrogen thus requires a non-negligible population of hydrogen atoms to be in the first excited ($n = 2$) state. It has long been realised that Ly α scattering in optically thick gas can enhance especially the $2p$ -level of HI (e.g. Pottasch 1960), which can lead to inverted level populations in the $2s_{1/2} - 2p_{3/2}$ transition (Field & Partridge 1961). Observational searches for 3-cm maser activity from nearby HII regions have not been successful, because Ly α pumping of hydrogen in nearby HII regions

is not effective enough to give rise to sufficient atomic hydrogen in its excited state.

In this paper we have shown that large HI column densities of primordial gas at $T \sim 10^4$ K, combined with a low molecular hydrogen abundance—which represent key requirements in the DCBH scenario—provide optimal conditions for pumping of the $2p$ -level of atomic hydrogen by trapped Ly α photons. We show that simplified models of the DCBH scenario give rise to a minimum optical depth through the 3-cm line, $\tau_{3\text{cm}} \sim -40$. We show that these models predict that CMB radiation passing through a cloud directly collapsing into a DCBH is amplified by up to a factor of $\sim 10^5$. For larger amplification factors the amplified CMB affects the $2p$ and $2s$ level populations such that further amplification is halted, and the maser saturates.

Hyperfine splitting of the 3-cm transition gives rise to a characteristic broad (FWHM \sim tens of MHz in the observer’s frame), asymmetric line profile, which is insensitive to the gas kinematics. The predicted signal subtends a small angular scale of $\sim 1 - 10$ mas, which translates to a the peak flux density in the range $0.3 - 3 \mu\text{Jy}$ with a line width of $\delta\nu \simeq 20$ MHz. This signal can be detected by using the spectral cube data from already-planned ultra-deep continuum and line surveys with SKA1-MID. This is remarkable, as it implies it may be possible to directly detect gas in emission in high-redshift ($z \sim 10 - 20$) from *individual* atomic cooling dark mater halos.

CR7, a recently discovered unusually luminous Ly α emitting source at $z \sim 6.6$ (Sobral et al. 2015), has been argued to be the first DCBH candidate (see Sobral et al. 2015; Pacucci & Ferrara 2015; Agarwal et al. 2015b). The large Ly α luminosity of CR7 implies a high escape fraction of Ly α photons. In contrast, we have shown that Ly α photons are destroyed through collisional processes when the 3-cm maser signal is maximized. Furthermore, the observed width of the Ly α spectral line (FWHM ~ 266 km s $^{-1}$, see Sobral et al. 2015) indicates that resonant scattering of Ly α photons - which broadens the Ly α spectral line (see Dijkstra 2014, and references therein) - is inconsistent with a scenario in which Ly α scatter $\log\langle N_{\text{scat}} \rangle \gtrsim 8$ (see Dijkstra & Gronke, in prep). This implies that if CR7 is indeed associated with

a DCBH, then it must represent an evolutionary stage during which there is no (detectable) stimulated 3-cm emission.

Our results were clearly obtained from a simplified representation of the DCBH scenario, which allowed us to focus entirely on identifying and modelling the relevant radiative processes. We stress that it is important to study these radiative processes in more realistic gas distributions especially because gas geometry can strongly affect the beaming of the maser, which affects the apparent angular scale of the masing cloud and therefore the predicted maser flux.

While challenges remain on the modelling side, we stress that it is well worth addressing these in future work, as the masing conditions that we found are uniquely associated with the physical conditions that enable the DCBH scenario: these conditions include chemically pristine gas (i.e. no dust) inside dark matter halos with $T_{\text{vir}} \sim 10^4$ K, in which molecular hydrogen formation and gas fragmentation have been suppressed. These last two additional requirements are important: ordinary pristine gas inside an atomically cooling halo would form H $_2$ during its collapse in quantities that are fatal for the required pumping of the maser levels. Similarly, once gas is allowed to fragment and clump, the radiative transfer of Ly α proceeds differently, with Ly α photons preferentially escaping through lower column density holes and scattering less frequently (see e.g. Neufeld 1991; Haiman & Spaans 1999; Gronke & Dijkstra 2014). The Ly α pumping efficiency is reduced in pristine environments *not* associated with the DCBH scenario. This implies that a detection of the redshifted 3-cm signature in deep SKA surveys would provide direct and unique evidence for the formation of supermassive black holes via the direct collapse of a gas cloud.

Acknowledgements MD thanks for the Raman Research Institute for their hospitality during a visit which started this project. We thanks Jonathan Pritchard, Max Gronke, Lluís Mas-Ribas for useful discussions, and Jens Chluba for helpful correspondence. This work was supported in part by NSF-grant AST-1312034 (for AL). We thank an anonymous referee for an excellent, constructive report.

REFERENCES

- Adams, T. F. 1972, ApJ, 174, 439
 Adams, T. F. 1975, ApJ, 201, 350
 Agarwal, B., Khochfar, S., Johnson, J. L., Neistein, E., Dalla Vecchia, C., & Livio, M. 2012, MNRAS, 425, 2854
 Agarwal, B., Davis, A. J., Khochfar, S., Natarajan, P., & Dunlop, J. S. 2013, MNRAS, 432, 3438
 Agarwal, B., Smith, B., Glover, S., Natarajan, P., & Khochfar, S. 2015a, arXiv:1504.04042
 Agarwal, B., Johnson, J. L., Zackrisson, E., et al. 2015b, arXiv:1510.01733
 Alcock, C., & Ross, R. R. 1985a, ApJ, 290, 433
 Alcock, C., & Ross, R. R. 1985b, ApJ, 299, 763
 Barkana, R., & Loeb, A. 2001, Phys. Rep., 349, 125
 Bolton, J. S., Haehnelt, M. G., Warren, S. J., et al. 2011, MNRAS, 416, L70
 Bonilha, J. R. M., Ferch, R., Salpeter, E. E., Slater, G., & Noerdlinger, P. D. 1979, ApJ, 233, 649
 Bromm, V., & Loeb, A. 2003, ApJ, 596, 34
 Chluba, J., & Sunyaev, R. A. 2009, A&A, 496, 619
 Condon, J. J. 1992, ARAA, 30, 575
 Cox, A. N. 2000, Allen’s Astrophysical Quantities, 1
 Dennison, B., Turner, B. E., & Minter, A. H. 2005, ApJ, 633, 309
 Dijkstra, M., Haiman, Z., & Spaans, M. 2006, ApJ, 649, 14
 Dijkstra, M., Haiman, Z., Mesinger, A., & Wyithe, J. S. B. 2008a, MNRAS, 391, 1961
 Dijkstra, M., Lidz, A., Pritchard, J. R., et al. 2008b, MNRAS, 390, 1430
 Dijkstra, M., & Loeb, A. 2009, MNRAS, 400, 1109
 Dijkstra, M., Ferrara, A., & Mesinger, A. 2014, MNRAS, 442, 2036
 Dijkstra, M. 2014, PASA, 31, e040
 Elitzur, M. 1990a, ApJ, 363, 628
 Elitzur, M. 1990b, ApJ, 363, 638
 Ershov, A. A. 1987, Soviet Astronomy Letters, 13, 115
 Fernandez, R., Bryan, G. L., Haiman, Z., & Li, M. 2014, MNRAS, 439, 3798

- Fan, X., Strauss, M. A., Schneider, D. P., Gunn, J. E., & et al. 2001, *AJ*, 121, 54
- Field, G. B. 1958, *Proceedings of the IRE*, 46, 240
- Field, G. B., & Partridge, R. B. 1961, *ApJ*, 134, 959
- Goldreich, P., & Keeley, D. A. 1972, *ApJ*, 174, 517
- Gronke, M., & Dijkstra, M. 2014, *MNRAS*, 444, 1095
- Haiman, Z., & Spaans, M. 1999, *ApJ*, 518, 138
- Haiman, Z., Spaans, M., & Quataert, E. 2000, *ApJL*, 537, L5
- Haiman, Z. 2013, *The First Galaxies*, 396, 293
- Harrington, J. P. 1973, *MNRAS*, 162, 43
- Hirata, C. M. 2006, *MNRAS*, 367, 259
- Hui, L., & Gnedin, N. Y. 1997, *MNRAS*, 292, 27
- Inayoshi, K., & Tanaka, T. L. 2015, *MNRAS*, 450, 4350
- Inayoshi, K., Haiman, Z., & Ostriker, J. P. 2015, *arXiv:1511.02116*
- Katz, N., Weinberg, D. H., & Hernquist, L. 1996, *ApJS*, 105, 19
- Latif, M. A., Schleicher, D. R. G., Schmidt, W., & Niemeyer, J. 2013, *MNRAS*, 433, 1607
- Latif, M. A., Bovino, S., Van Borm, C., et al. 2014, *MNRAS*, 443, 1979
- Latif, M. A., Bovino, S., Grassi, T., Schleicher, D. R. G., & Spaans, M. 2015, *MNRAS*, 446, 3163
- Latif, M. A., & Volonteri, M. 2015, *MNRAS*, 452, 1026
- Li, Y., Klessen, R. S., & Mac Low, M.-M. 2003, *ApJ*, 592, 975
- Lusso, E., Comastri, A., Simmons, B. D., et al. 2012, *MNRAS*, 425, 623
- Marconi, A., Risaliti, G., Gilli, R., et al. 2004, *MNRAS*, 351, 169
- Mortlock, D. J., et al. 2011, *Nature*, 474, 616
- Myers, P. C., & Barrett, A. H. 1972, *ApJ*, 176, 111
- Neufeld, D. A. 1990, *ApJ*, 350, 216
- Neufeld, D. A. 1991, *ApJL*, 370, L85
- Omukai, K., Tsuribe, T., Schneider, R., & Ferrara, A. 2005, *ApJ*, 626, 627
- Omukai, K., Schneider, R., & Haiman, Z. 2008, *ApJ*, 686, 801
- Osterbrock, D. E., & Ferland, G. J. 2006, *Astrophysics of gaseous nebulae and active galactic nuclei*, 2nd. ed. by D.E. Osterbrock and G.J. Ferland. Sausalito, CA: University Science Books, 2006,
- Pacucci, F., & Ferrara, A. 2015, *MNRAS*, 448, 104
- Pallottini, A., Ferrara, A., Pacucci, F., et al. 2015, *arXiv:1506.07173*
- Pottasch, S. R. 1960, *ApJ*, 131, 202
- Regan, J. A., Johansson, P. H., & Wise, J. H. 2014, *ApJ*, 795, 137
- Rybicki, G. B., & Lightman, A. P. 1979, *New York, Wiley-Interscience*, 1979. 393 p.,
- Scholz, T. T., Walters, H. R. J., Burke, P. J., & Scott, M. P. 1990, *MNRAS*, 242, 692
- Scholz, T. T., & Walters, H. R. J. 1991, *ApJ*, 380, 302
- Sethi, S. K., Subrahmanyan, R., & Roshi, D. A. 2007, *ApJ*, 664, 1
- Sethi, S., Haiman, Z., & Pandey, K. 2010, *ApJ*, 721, 615
- Shang, C., Bryan, G. L., & Haiman, Z. 2010, *MNRAS*, 402, 1249
- Shapiro, P. R., & Kang, H. 1987, *ApJ*, 318, 32
- Sobral, D., Matthee, J., Darvish, B., et al. 2015, *ApJ*, 808, 139
- Spaans, M., & Silk, J. 2006, *ApJ*, 652, 902
- Spaans, M., & Norman, C. A. 1997, *ApJ*, 488, 27
- Spitzer, L., Jr., & Greenstein, J. L. 1951, *ApJ*, 114, 407
- Strehlitski, V. S., Ponomarev, V. O., & Smith, H. A. 1996, *ApJ*, 470, 1118
- Sugimura, K., Omukai, K., & Inoue, A. K. 2014, *MNRAS*, 445, 544
- Thoul, A. A., & Weinberg, D. H. 1995, *ApJ*, 442, 480
- Van Borm, C., & Spaans, M. 2013, *A&A*, 553, L9
- Venemans, B. P., Findlay, J. R., Sutherland, W. J., et al. 2013, *ApJ*, 779, 24
- Visbal, E., Haiman, Z., & Bryan, G. L. 2014a, *MNRAS*, 442, L100
- Visbal, E., Haiman, Z., & Bryan, G. L. 2014b, *MNRAS*, 445, 1056
- Volonteri, M., & Bellovary, J. 2012, *Reports on Progress in Physics*, 75, 124901
- Wild, J. P. 1952, *ApJ*, 115, 206
- . 2009, *AJ*, 137, 3541
- Wolcott-Green, J., Haiman, Z., & Bryan, G. L. 2011, *MNRAS*, 418, 838
- Wouthuysen, S. A. 1952, *AJ*, 57, 31

APPENDIX

VERIFYING THE DOMINANCE OF STIMULATED EMISSION

We approximated Eq 1

$$I_\nu(s) = I_{\nu,0}e^{-\kappa_\nu s} + \frac{j_\nu}{\kappa_\nu} (1 - e^{-\kappa_\nu s}) \approx I_{\nu,0}e^{-\kappa_\nu s}, \quad (\text{A1})$$

which is valid only when

$$I_{\nu,0} \gg \left| \frac{j_\nu}{\kappa_\nu} \right|. \quad (\text{A2})$$

This section shows this condition is generally met throughout our calculations. If we substitute the definitions of κ_ν and j_ν (see Eq 4) we get

$$\frac{j_\nu}{\kappa_\nu} = \frac{2\nu^3 h}{c^3 \left(\frac{g_u n_l}{g_l n_u} - 1 \right)} = \frac{2E_{\text{FS}}}{\lambda_{\text{FS}}^2 \left(\frac{g_u n_l}{g_l n_u} - 1 \right)}, \quad (\text{A3})$$

where in the second step we choose to evaluate this at line centre of the fine-structure transition (i.e. $\nu = \nu_{\text{FS}}$, $\lambda = \lambda_{\text{FS}}$). Eq A2 can therefore be rephrased as

$$\frac{2kT_{\text{CMB}}}{\lambda_{\text{FS}}^2} \gg \left| \frac{2E_{\text{FS}}}{\lambda_{\text{FS}}^2 \left(\frac{g_u n_l}{g_l n_u} - 1 \right)} \right|, \quad (\text{A4})$$

which can be simplified to

$$\frac{kT_{\text{CMB}}}{E_{\text{FS}}} \gg \left| \frac{1}{\left(\frac{g_u n_l}{g_l n_u} - 1 \right)} \right| \quad (\text{A5})$$

Since $T_{\text{CMB}} = 2.725(1+z)$ K, and $E_{\text{FS}}/k \sim 0.5$ K for the 3-cm transition, and ~ 0.05 K for the 27-transition. When we have stimulated emission we have $n_u \gg n_l$, and the R.H.S is 1. In case there is stimulated emission, the left-hand

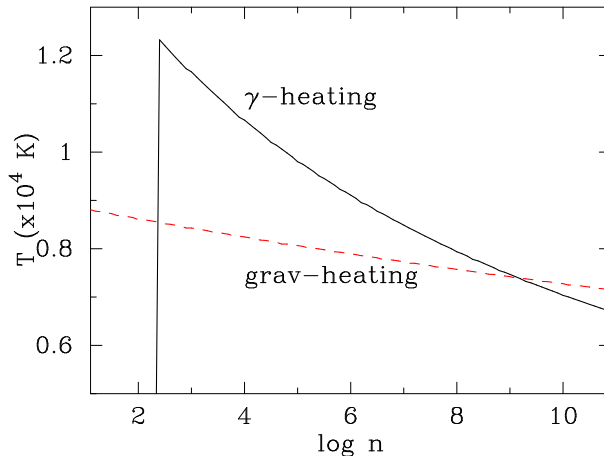


FIG. 8.— The temperature evolution in the gravitational heating model (*red dashed line*), and radiative heating with $H^\gamma = 10^{43}$ erg s^{-1} (*black solid line*). In the radiative heating case, the total heating - and therefore cooling - rate is constant. As density increases the temperature decreases to maintain a constant total cooling rate. The density-dependence of T in the gravitational heating model is weaker because the heating rate increases with density.

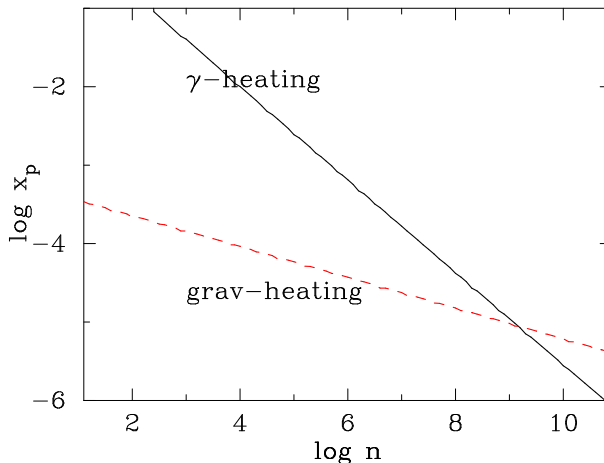


FIG. 9.— Same as Fig 8, but now we show the ionised fraction $x_p = x_e$. In the radiative heating case, the gas becomes fully ionised at $n < n_{\text{crit}} \sim 240 \text{ cm}^{-3}$ (see Eq 16), and the ionised fraction goes to 1. side is clearly much greater than the right hand side and our approximation for the solution of the radiative transfer equation is valid.

INTERMEDIATE QUANTITIES

Figures 8-10 show intermediate results of our calculation. Figure 8 shows the density-dependence of T for the gravitational heating model (*red dashed line*) and radiative heating model with $H^\gamma = 10^{43}$ erg s^{-1} (*black solid line*). In the radiative heating case, the cooling rate is constant, $L_{\text{cool}} \propto n$ (see § 3.1). To maintain a constant total cooling rate the temperature must decrease. The density-dependence of T in the gravitational heating model is weaker because the cooling rate increases with density as $L_{\text{cool}} \propto n^{5/3}$ (see § 3.1).

Figure 9 shows the density-dependence of the associated ionised fraction $x_e = x_p \equiv n_p/n$. The different density dependence of x_p between both models is driven entirely by the different temperature evolution. Because in the model with radiative heating the cloud is fully ionised for $n < n_{\text{crit}} \sim 240 \text{ cm}^{-3}$, the ionised fraction goes to unity.

Finally, the *left panel* of Figure 10 shows the density-dependence of $\langle N_{\text{scat}} \rangle$. For the gravitational heating model we have¹⁰ $\langle N_{\text{scat}} \rangle \propto \tau_0 \propto n^{2/3}$. For $\log n \gtrsim 5.6$, collisional deexcitation limits $\langle N_{\text{scat}} \rangle$ and it decreases as $\langle N_{\text{scat}} \rangle \propto n_p^{-1} \propto n^{-0.8}$. For the model with radiative heating $\langle N_{\text{scat}} \rangle = 0$ for $n < n_{\text{crit}}$ as the gas is fully ionised. It rises to catch up with $\langle N_{\text{scat}} \rangle$ for the gravitational model, as the column densities become increasingly similar for both models as n increases above $n > n_{\text{crit}}$. However, because of the larger ionised fraction in the radiative heating models, collisional deexcitation becomes important at lower density and $\langle N_{\text{scat}} \rangle$ decreases. $\langle N_{\text{scat}} \rangle$ is equal for both models at the density

¹⁰ The actual density dependence is slightly steeper than this,

because $\tau_0 \propto N_{\text{HI}} T^{-1/2}$, and T decreases with n , albeit slowly.

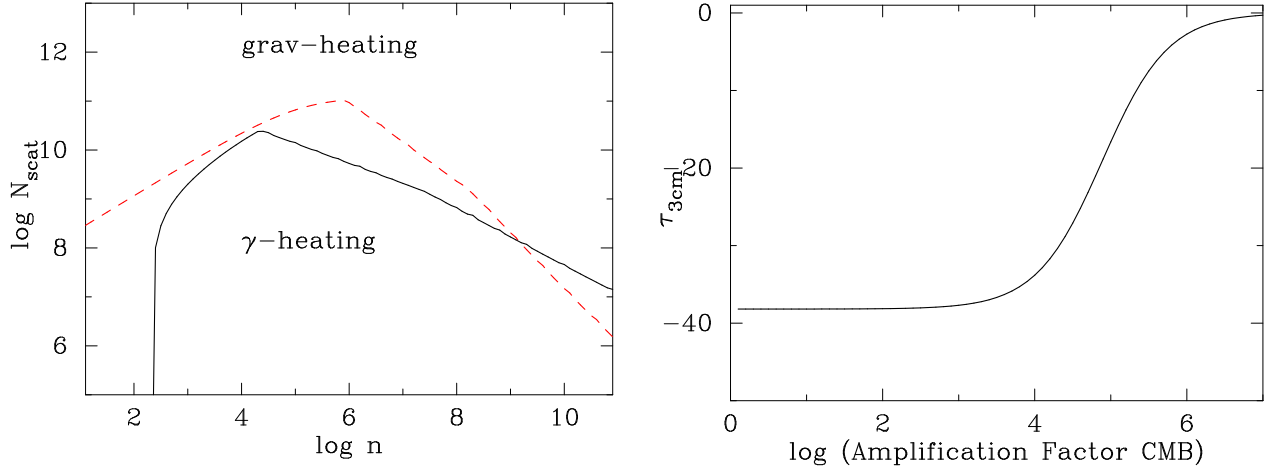


FIG. 10.— *Left*: Same as Fig 8, but now we show $\langle N_{\text{scat}} \rangle$. For both cases $\log(N_{\text{scat}}) \sim 8 - 11$. The quantitative behaviour of both curves is discussed in the text. We have also indicated at what the number density the fine structure optical depth reaches its minimum. *Right*: This plot shows the optical depth in the 3-cm transition as a function of CMB-amplification factor. Stimulated emission from the amplified CMB reduces the $2p$ -level population, and hence the absolute value of $\tau_{3\text{cm}}$, only when the CMB is amplified more than a factor of $\sim 10^5$. Maser saturation is not important up until these amplification factors.

where the gas has the same T .

MASER SATURATION

As the CMB is amplified by a factor of B_{CMB} through the cloud collapsing into/onto a DCBH, the CMB induced transitions between the $2p$ and $2s$ levels increase by this same factor. Our original calculations did not account for this boost. Here, we repeat our calculations for the radiative heating model with $H\gamma = 10^{43} \text{ erg s}^{-1}$, at a fixed number density $\log n \sim 7$, but boost the CMB-induced radiative transitions by a factor of B_{CMB} , i.e. $\Gamma_{2s2p}^{\text{CMB}} \rightarrow B_{\text{CMB}}\Gamma_{2s2p}^{\text{CMB}}$ and $\Gamma_{2p2s}^{\text{CMB}} \rightarrow B_{\text{CMB}}\Gamma_{2p2s}^{\text{CMB}}$. The *right panel* of Figure 10 shows $\tau_{3\text{cm},0}$ as a function of B_{CMB} . This plot shows that stimulated emission by the CMB starts affecting the $2p$ -levels only when $B_{\text{CMB}} \sim 10^5$, because only then does the de-population rate via stimulated emission become comparable to the population rate through Ly α scattering.

SOME USEFUL NUMBERS

We can verify the magnitude of our calculations by comparing the cross-section for stimulated 3-cm transition to that of some known electronic transition. We generally have

$$\kappa_\nu = \kappa(\nu) = \frac{h\nu_{ul}B_{ul}}{4\pi\Delta\nu_{ul}} \times \left(\frac{g_u}{g_l}n_l - n_u \right) \phi(\nu). \quad (\text{D1})$$

We will now evaluate the cross-section in some transitions based on this.

1. For Ly α we have $n_u \ll n_l$, $g_u = 3$, $g_l = 1$, $A_{ul} = 6.25 \times 10^8 \text{ s}^{-1}$, and $\phi(\nu_\alpha) = 1/\sqrt{\pi}$. This gives us

$$\sigma_0 = \frac{\kappa(\nu_\alpha)}{n_{1s}} = \frac{3}{8\pi} \frac{\lambda_\alpha^2 A_\alpha}{\sqrt{\pi} \Delta\nu_\alpha} = 5.89 \times 10^{-14} (T/10^4)^{-1/2} \text{ cm}^{-2}, \quad (\text{D2})$$

which is a familiar result (see e.g. Dijkstra 2014).

2. For H α the velocity averaged cross-section can be computed similarly. However, we take a short cut and point out that

$$\sigma_{0,\text{H}\alpha} = \sigma_0 \left(\frac{f_{\text{H}\alpha} \lambda_{\text{H}\alpha}}{f_{\text{Ly}\alpha} \lambda_{\text{Ly}\alpha}} \right) = 4.86 \times 10^{-13} (T/10^4)^{-1/2} \text{ cm}^{-2}, \quad (\text{D3})$$

where $\lambda_{\text{Ly}\alpha} = 1215.67 \text{ \AA}$, $\lambda_{\text{H}\alpha} = 6562.8 \text{ \AA}$, and the oscillator strengths $f_{\text{Ly}\alpha} = 0.416$ and $f_{\text{H}\alpha} = 0.637$.

3. For stimulated 3-cm Eq 4 shows that (for $n_u \gg n_l$)

$$\sigma_{3\text{cm},0} = -\frac{\lambda^2 A_{ul}}{2\pi A_\alpha} = -2.0 \times 10^{-15} \text{ cm}^2, \quad (\text{D4})$$

where the negative sign reflects the negative opacity of the inverted level population. Comparing the last two numbers we get

$$\frac{\tau_{0,\text{H}\alpha}}{\tau_{3\text{cm},0}} = \frac{3}{2} \frac{\sigma_{0,\text{H}\alpha}}{\sigma_{3\text{cm},0}} \approx -362(T/10^4 \text{ K})^{-1/2} \quad (\text{D5})$$

where the factor 3/2 represents the fraction of atoms in the $2p$ state that is in the $2p_{3/2}$ state. We note that this is a factor of $\sim \sqrt{2}$ lower than the number given in Field & Partridge (1961), who find that $\frac{\tau_{0,\text{H}\alpha}}{\tau_{3\text{cm},0}} \sim -700$ for $T = 5000 \text{ K}$ (they adopt $v_{\text{th}} = 9.1 \text{ km s}^{-1}$). The origin of this (small) difference is unclear.

LY α DESTRUCTION BY MOLECULAR HYDROGEN

Neufeld (1990) provides an expression for the escape fraction of Ly α photons from a slab of gas with center-to-edge column density N_{HI} , and that contains a molecular hydrogen fraction $f_{H_2} \equiv n_{H_2}/n_{\text{H}}$. This expression is

$$f_{\text{esc}}^{H_2}(\tau_0) = \frac{4}{\pi} \sum_{n=1}^{\infty} \frac{(-1)^{n-1} [(2n-1) + (\sqrt{6}\epsilon_a\tau_0/\pi)(1-x_n)]}{A_n},$$

$$A_n = (2n-1)[(2n-1) + \sqrt{6}(\epsilon_a + \epsilon_0)\tau_0/\pi] + (6\epsilon_a\epsilon_0\tau_0^2/\pi^2)(1-x_n^2) \quad (\text{E1})$$

, where $x_n = \exp(-\pi(n - \frac{1}{2})\sigma_a/\tau_0)$, and

$$\sigma_a = 8.3 \times 10^5 T_4^{-1}, \quad \epsilon_0 = 0.082 \times f(2,6) \times f_{H_2}, \quad \epsilon_a = 0.069 \times f(2,5) \times f_{H_2}, \quad (\text{E2})$$

in which $f(2,5)$ and $f(2,6)$ denote the fraction of H_2 atoms in the $v = 2, J = 5$ state and $v = 2, J = 6$ state. We adopt $\log f(2,5) = -1.8$ and $\log f(2,6) = -2.4$ from Figure 19 of Neufeld (1990). These numbers assume LTE.

OTHER LY α DESTRUCTION MECHANISM

1. Photoionization from the $2p$ -level by the quasar: The radiative heating models contain a luminous source in the centre of the cloud. Hydrogen atoms in the $2p$ can be photoionized by photons with $E > 3.4 \text{ eV}$, which can penetrate into the neutral gas. This photoionisation rate can be estimated from

$$\Gamma_{\text{ion}}^{2p} = \dot{N}_{2p\text{-ion}} \frac{\langle \sigma_{\text{ion}} \rangle}{4\pi r^2}, \quad (\text{F1})$$

where $\dot{N}_{2p\text{-ion}}$ denotes the rate at which photons in the energy range $E = 3.4 - 13.6 \text{ eV}$ are produced, $\langle \sigma_{\text{ion}} \rangle$ denotes the frequency averaged cross-section. Substituting some numbers gives:

$$\Gamma_{\text{ion}}^{2p} = 0.1 \left(\frac{\dot{N}_{2p\text{-ion}}}{10^{54} \text{ s}^{-1}} \right) \left(\frac{r}{1 \text{ pc}} \right)^{-2} \text{ s}^{-1} \quad (\text{F2})$$

where we assumed that $\langle \sigma_{\text{ion}} \rangle = 1.4 \times 10^{-17} \text{ cm}^{-2}$. For comparison, the cloud radius at the minimum τ_{FS}^0 is $\sim 3 \text{ pc}$ is $R_{\text{cl}} \sim 2 \text{ pc}$, at which $\log x_p \sim -3.8$, and the collisional deexcitation rate is $C_{2p2s} n_p \sim 0.5 \text{ s}^{-1}$. That is, photoionization from the $2p$ state can be important in the inner parts of the cloud in the radiative heating case, but is not a show-stopper.

2. Photodetachment of H^- . Ly α photons can detach the electron from the H^- ion. The cross-section for this process is $\sigma = 5.9 \times 10^{-18} \text{ cm}^{-2}$ (e.g. Shapiro & Kang 1987) for Ly α photons, which is almost an order of magnitude larger than the photoionisation cross-section from the $n = 2$ level. So, unless the H^- number density exceeds $0.1[n_{2p} + n_{2s}]$, we do not consider this process important. Some numbers, for radiative heating we reach the minimum in τ for $\log n \sim 7$, where we have $\log n_{2p} \sim -2.6$. We thus have a fractional number density of $\log n_{2p}/n \sim -9.6$, while one-zone models indicate a H^- fraction a bit below $\log n_{H^-}/n \sim -11$ (Latif et al. 2014). In other words, photo detachment of H^- is not negligible, but it is slightly less important than photoionization from the $n = 2$ level, which is included in our calculations. Similar, for the gravitational heating model we have $\log n_{2p}/n \sim -10.7$ at the minimum for $\log n \sim 9$, while $\log n_{H^-}/n \sim -12$ (Latif et al. 2014). In addition, the destruction of Ly α photons via photoionization from the $n = 2$ level is negligible compared to the destruction due to collisional mixing of the $2p$ and $2s$ levels at the densities where we have the strongest maser activity.